

Dear Reviewer#3,

Thank you very much for your third review of our manuscript. Please find below our replies to your comments. Note that your comments are written in blue while our replies are black.

Reply to your comments of 02 January 2020

Onken et al. Very high-resolution modelling of submesoscale turbulent patterns and processes in the Baltic Sea; Ocean Sci. Discuss., <https://doi.org/10.5194/os-2019-44>

Review 3

Final comments

(1) I am not satisfied with the response of the authors to some of my previous comments and questions. The major problems are related to the authors' concept that the internal waves are part of submesoscale processes

Action: see below (5)

(2) and the set-up of models – too low number of vertical layers,

In our previous reply to your comments of 20 September 2019, we have justified the number of vertical levels at length in item (20). You may note as well that for technical reasons the number of sigma-layers in a ROMS-to-ROMS nesting must not change. Hence, the number of layers in R100 is the same as in R500.

Action: none

(3) nesting of models with and without atmospheric forcing,

This issue was already discussed in detail in our previous reply to your comments of 18 July 2019. We are surprised that you raise it up again as you seemed to be satisfied according to your comments of 20 September.

Action: none

(4) different turbulent parametrization, etc.

As far as we can see, the different parameterisations were never criticized by you – nor by your comments of 18 July, nor by those of 20 September.

Action: none

(5) The authors refer to a paper by McWilliams (2016) to support their approach that internal waves are also among the submesoscale turbulent patterns and processes. At the same time, Williams (2016) clearly distinguishes between the internal gravity waves (IGW) and submesoscale currents (SMC). The scales of SMC and IGW are coinciding, but they are two separate branches of the flow of energy from mesoscale processes to microscale dissipation. Although in the term “submesoscale processes”, the scale is mentioned, it is more than that. See, e.g., a definition by McWilliams (2019): “Besides their identifying scales, submesoscale currents are distinctive in their flow

patterns, their essential dynamical processes, and their consequences for transport, mixing, and dissipation in the general circulation". I think it is misleading to define internal waves and submesoscale processes as submesoscale turbulent patterns and processes. It also causes a misleading statement that submesoscale processes are characterized by strong vertical speeds of $O(100 \text{ m day}^{-1})$.

OK – we agree: after a thorough rereading of McWilliams (2016), we found in the Introduction “This SMC scale range overlaps to a high degree with IGWs, and the two phenomena must be distinguished by their evolutionary behaviors,...”

Action:

- The corresponding piece of text in the Introduction was rephrased (new ms P2L25-26)
- A paragraph in the Conclusions was rewritten (P22L3-9)
- $O(100) \text{ m day}^{-1}$ was substituted by $O(10) \text{ m day}^{-1}$ in the Abstract (P1L10)

(6) Since some questionable assumptions were used and clearly different settings were applied to the nested models, readers still might wonder what results are of general value and what results are related to the approach. For instance, the authors state that the submesoscale features appear preferably in the shallow areas with water depths less than 40 m. Is it a natural phenomenon or is it related to the model resolution? One could argue that in the deeper areas, the vertical resolution of the model is too coarse to simulate submesoscale processes.

According to McWilliams (2019), the principal SMC generation mechanisms are (1) extraction of available potential energy in the weakly stratified surface layer (“mixed-layer instability”), and (2) topographic-drag vorticity generation in flows along a sloping bottom. As strong bottom slopes are found only along Rönnebank and in the south of the R100 domain (see Fig. 1), the mechanism (2) may be significant in those areas. However, for water depths $> 50 \text{ m}$, the bottom is mostly flat and topographic-drag vorticity generation can be excluded. Hence, mixed-layer instability is the only generation mechanism there, and that does not require higher vertical resolution.

Action:

- The enhanced submesoscale activity in shallow areas is discussed (P12L29-P13L2)
- McWilliams (2019) was added to the References

(7) There are also smaller issues, which could be omitted to allow to shorten and focus the manuscript better. For instance, it is not relevant to discuss the long-term precipitation and evaporation to justify why salinity is an ideal parameter (passive tracer), etc.

Remember that **you** asked both in your reviews of 18 July (item (9)) and 20 September (item (8)) for an explanation why salinity is the ideal parameter.

Action: The corresponding discussion was slightly shortened. See P7L15-17.

On the other hand, the authors have conducted a thorough analysis of their results using a series of parameters and their distributions related to certain processes, patterns or mechanisms and compared the findings with other papers/authors. Thus, I think the paper is worth to be published to intensify the discussions on the nature and features of submesoscale processes. I leave the decision to the Editor(s).

McWilliams J.C. 2016. Submesoscale currents in the ocean. *Proc. R. Soc. A* 472: 20160117. <https://doi.org/10.1098/rspa.2016.0117>.

McWilliams J.C. 2019. A survey of submesoscale currents. *Geosci. Lett.* 6:3.
<https://doi.org/10.1186/s40562-019-0133-3>.

Dear Reviewer#4,

Thank you very much for your review of our manuscript. Please find below our replies to your comments. Note that your comments are written in blue while our replies are black. P(age) and L(ine) numbers refer to the new manuscript (ms) except for if otherwise stated.

Our replies below are ordered alphabetically (A), (B), (C), ... in contrast to our replies to your comments of 7 October which were ordered (1), (2), (3)

Reply to your comments of 27 November 2019

Referee report of the re-revised manuscript “Very high-resolution modelling of submesoscale turbulent patterns and processes in the Baltic Sea” (version of 12 Nov 2019) by Reiner Onken, Burkard Baschek, and Ingrid M. Angel-Benavides, submitted for consideration to Ocean Science.

I would like to thank the authors for their reply and the changes implemented to the manuscript. Unfortunately, some points in their reply have left me uneasy. My most major concern about this manuscript was and still is the modelling methodology. I was surprised by some of their choices and asked the authors to better justify them or explain the process which lead to those choices. For some issues they did so, for which I thank them. But for other chose not to do so, and for some issues I did not find their justifications convincing.

As sound methodology is one of the most important aspects of any scientific study, it is of utmost importance that modellers do their due diligence when designing modelling experiments. I am not yet convinced this has been the case in this study. Therefore I have no choice but to recommend another major revision. I hope the authors would take some time to think what can be considered a “reasonable effort” on their part to make sure they can justify their choices adequately, and whether they feel confident that their modelling configuration is well enough documented in the manuscript, along with any potential weaknesses. I emphasize that I do not claim that there necessarily are any fundamental flaws in the methodology, but rather that their replies (and in some cases the lack thereof) have left me with insufficient information to determine if this is so.

Please find my specific comments below. Numerals in parenthesis refer to the replies made by the authors in response to my original review. At this time I refrain from making what I would consider minor comments so they do not shadow these more major issues.

(A) In their reply, the authors do not address in any way my three main comments presented under “General comments”. I was truly surprised by this decision. These were the questions I was most looking to be answered, but there are no answers. Because of this I feel I lack information to make a fully informed review. Their other replies do not really address these comments fully.

Please find our replies below.

(B) Regarding my first major comment asking the paper’s objectives to be clarified, I see that there have been some edits to the introduction. On one hand I feel this comment could have been addressed more carefully. However, if the authors find their manuscript now accessible enough and do not want to address this in more depth, I have no further comments on this issue.

Action: The corresponding paragraph in the Introduction was rewritten: P2L1-8.

(C) Regarding my second and third point about documenting the limitations of the study and

justifying their methodology, I see improvement and that needs to be acknowledged. However, I feel it would have been possible for the authors to be much clearer on this issue.

Concerning the limitations of the study, we have added or modified pieces of text in the Conclusions and in the Abstract.

Action: see P21L30-P22L2 and P1L6-9

(D) For example, regarding their reply (8), I don't think that "worrying the readers" is an acceptable reason to omit information that would help the readers make their own conclusions about the study.

Action: According to your desire in the previous review, we have expanded the description of the CMEMS product in Section 2.2, see P5L8-16.

(E) This approach of omitting information is deeply worrying and leaves me to wonder what else has been omitted from the manuscript because the readers would find it upsetting.

This remark is speculative, polemic, and provocative.

Action: none

(F) Also regarding reply (8), I would again ask the authors to insert into the text the version number of the CMEMS product they used. This version number is identified on the cover of the product user manual (and in the following change record) as e.g. "4.0" or "3.0". The issue of the user manual is useful information, but it is not the same thing as the version of the product.

At the time when we started the modeling activities in 2017, the PUM version was 2.1.

Action: see P5L12

(G) In their reply (9), the authors indicate they have not really done any kind of survey of available boundary condition products before settling on the CMEMS product, or indeed even considered other options. They also say they "cannot remember" if the reanalysis product was available at that time. In my opinion, "due diligence" or "reasonable care" would have required at least rudimentary survey of available state-of-the-art options for boundary data, along with their main features. I sincerely hope this reply was some kind of misunderstanding, perhaps due to linguistic challenges.

No - it was **not** some kind of misunderstanding. We checked again the Product User Manual of BALTICSEA_REANALYSIS_PHY_003_011 and found on P5/16 that the product was released in April 2018, hence it was not yet available when we started our modeling activities in early 2017. The coarse horizontal resolution of 4 km would also have required a triple-nesting setup (4 km --> 800 m --> 267 m --> 89 m) in order to arrive at a resolution of 100 m because a nesting ratio of 5 should not be exceeded, and the ratio should be uneven (i.e. 5 or 3) for the ROMS-to-ROMS nesting. To the best of our knowledge, there was no alternative to CMEMS-HBM in 2017, and a *rudimentary survey of available state-of-the-art options for boundary data, along with their main features* was not required.

Action: A few remarks concerning the choice of CMEMS-HBM have been added (P5L21-23)

(H) In their reply (10) they state that they did not do any effort to obtain the bathymetric data of their boundary data. In fact, they still have not done so after being asked about this by myself and earlier by another referee. Rather, in their reply they just state their assumption on what this file

“probably” is. Yet they still cite the lack of this file as a rationale for their nesting procedures in the manuscript. In my opinion, in this case a reasonable requirement would have been at least one email asking for this file from the service desk. If they do not provide it after asking, fine. If the file is not useful for whatever reason, then that’s fine too. But I do not understand why no effort was taken to obtain it, especially after the comments made by one of the other reviewers.

We have investigated again the issue with the bathymetry data and found that *the file would not have been useful for whatever reason*. For justification, we explain now step by step the downscaling procedure, starting from CMEMS-HBM where all prognostic variables are vertically interpolated from the HBM native grid onto standard depth levels:

- (1) The CMEMS-HBM fields are interpolated horizontally on the higher-resolution R500 grid, but still on the same standard depth levels.
- (2) All fields (except for the sea surface height) are interpolated vertically on the ROMS terrain-following vertical coordinates, the depth of which is determined *solely* by the ROMS-bathymetry. This bathymetry was already iteratively smoothed until the stability condition of Haidvogel et al. (2000) was reached everywhere.
- (3) The vertical interpolation of the horizontal velocities u and v is not mass conserving, if CMEMS-HBM provides non-zero normal velocities close to topographic obstacles which are present in ROMS but not in HBM. If these velocities hit, for instance, a seamount, the the continuity equation in ROMS would create unrealistic vertical velocities.
- (4) Such an issue occurred once in R500 at the northern domain boundary. There, the meridional velocity flew against a small abyssal hill that was apparently not existent in HBM. To cure that problem, the hill was flattened manually until the vertical velocities diminished.

As you can see, we could not have made use of the HBM bathymetry.

Action:

- The critical sentence in the old ms (P5L22-23) was removed.
- The text in bullet 4 was modified (P6L17-20).

(I) If we take replies (8), (9) and (10) together, they leave the impression that the authors have decided to use the CMEMS product as their boundary data without much consideration for its features, and now do not want to explain their choice or the main features of the dataset in the paper. This impression may very well be unintended, but I would kindly suggest to the authors to reconsider if it would in fact be better to just briefly explain these things to the readers to avoid such misunderstandings.

Action: see above **(D), (E), (F), (G), (H)**

(J) Based on my experience from the ocean modelling community, it is not accurate at all to call these model configurations “expensive in terms of computer resources” in the year 2019. Their reply (13) justifies this by claiming that this is a matter of opinion, but frankly, the given information seems to indicate that this model is not computationally expensive when compared to other commonly used configuration. This can be e.g. regional CMEMS configurations, or recently published coastal modelling configurations from the Baltic Sea basin. It is also run on a relatively modest computational system. The test phase of 3 months seems very much normal for this kind of a study, not exceptionally long at all. I ask the authors to remove this statement from the manuscript.

Action: The statement was removed. See P9L14.

Very high-resolution modelling of submesoscale turbulent patterns and processes in the Baltic Sea

Reiner Onken¹, Burkard Baschek¹, and Ingrid M. Angel-Benavides¹

¹Helmholtz-Zentrum Geesthacht, Max-Planck-Straße 1, 21502 Geesthacht, Germany

Correspondence to: Reiner.Onken@hzg.de

Abstract. In order to simulate submesoscale turbulent patterns and processes (STPPs) and to analyse their properties and dynamics, the Regional Ocean Modeling System (ROMS) was run for June 2016 in a subregion of the Baltic Sea. To create a realistic mesoscale environment, ROMS with 500-m horizontal resolution (referred to as R500) is one-way nested into an existing operational model, and STPPs with horizontal scales < 1 km are resolved with a second nest of 100-m resolution (R100). Both nests use 10 terrain-following layers in the vertical. The comparison of the R500 results with a satellite image shows fair agreement. While R500 is driven by realistic air-sea fluxes, the atmospheric forcing is turned off in R100 because it prevents the generation of STPPs and blurs submesoscale structures. Therefore, R100 provides a deep insight into ageostrophic processes and associated quantities ~~when the atmospheric forcing is turned off~~ under quasi-adiabatic conditions that are approximately met in no-wind or light-wind situations. The validity of the results is furthermore limited to the selected region and the time of the year. STPPs evolve rapidly within a about a day. They are characterised by ~~strong~~ vertical speeds of $\mathcal{O}(100)$ m day⁻¹ and relative vorticities and divergences reaching multiple of the Coriolis parameter. Typical elements of the secondary circulation of two-dimensional strain-induced frontogenesis are identified at an exemplary front in shallow water, and details of the ageostrophic flow field are revealed. The conditions for inertial and symmetric instability are evaluated for the whole domain, and the components of the tendency equation are computed in a subregion. While anticyclonic eddies are generated solely along coasts, cyclonic eddies are rolled-up streamers and found in the entire domain. A special feature of the cyclones is their ability to absorb internal waves and to sustain patches of continuous upwelling for several days favouring plankton growth. The kinematic properties show good agreement with observations, while some observed details within a small cyclonic eddy are only partly reproduced, most likely due to a lack of horizontal resolution or non-hydrostatic effects.

1 Introduction

This article was motivated by the “Expedition Clockwork Ocean” which was conducted 20–28 June 2016 in the ~~western~~ Baltic Sea to the south of the island of Bornholm. The objective of that survey was to observe submesoscale turbulent patterns and processes (STPPs) in order to better understand their role in the cascade of turbulent kinetic energy in the ocean, and to assess their impact on the primary production.

Presently, the knowledge about STPPs in the corresponding area is primarily limited to eddy statistics and originates solely from space-borne remote sensing observations (Gurova, 2012; Tavri et al., 2016; ?) and the model study of Vortmeyer-Kley et al. (2019). Some more information about kinematic properties of STPPs is conveyed by the high-resolution numerical study of Zhurbas et al. (2019), who showed that the overwhelming dominance of cyclonic eddies on satellite images is related to their higher angular velocity, more pronounced differential rotation, and a negative helicity. In the following, high-resolution modeling is used to ~~create and characterise such STTPs~~ generate STTPs and to further improve our knowledge about their characteristics (i.e. tracer patterns, kinematics, impact of atmospheric forcing, fronts, instabilities, and eddies), in the corresponding region at the respective time ~~for later comparison with the observed features~~.

Submesoscale turbulence is characterised by horizontal scales between 10 m and 10 km, vertical scales from 1 to 100 m, and time scales from hours to days (McWilliams, 2016). Thus, in the turbulence spectrum of the ocean, the submesoscale occupies 4 orders of magnitude in the horizontal, 3 orders in the vertical, and 3 orders of magnitude in time. As the whole spectrum of horizontal motions extends over 9 orders of magnitude between the basin-scale circulation (10^6 m) and the dissipation scale (10^{-2} m, see Müller et al. (2005)), a significant fraction of the spectrum is occupied by the submesoscale. The submesoscale wavenumber band is the intermediate regime between the mesoscale and the microscale (McWilliams, 2008); it separates the larger-scale flow, where the Coriolis force dominates (Rossby number, $Ro < 1$), from the smaller scales where the rotation of the Earth is of minor importance ($Ro \sim \mathcal{O}(1)$).

The energy sources for ocean currents are mainly at the planetary scale ($\mathcal{O}(1000$ km)), while the energy is removed at the microscale by viscous dissipation of kinetic energy where it is finally converted to heat. In order to equilibrate the ocean on climatological time scales, this demands a continuous spectral flow from the planetary scale to the microscale, which is called the “blue” cascade. However, according to the theory of geostrophic turbulence (Charney, 1971; Rhines, 1979), the energy cascade in low Rossby number regimes is “red”, i.e. there is a feedback of energy from mesoscale turbulence to larger scales. This leads to the question how the mesoscale energy is dissipated. A generic answer was given by McWilliams (2016): “Submesoscale currents spontaneously emerge from mesoscale eddies and boundary currents, especially in the surface and bottom boundary layers. They are generated through instabilities, frontogenesis and topographic wakes” leading to the required forward cascade.

The elements of submesoscale turbulence are essentially the same as in mesoscale turbulence: fronts, instabilities, meanders, eddies, ~~filaments, and—in addition—internal waves~~ and filaments. However, the submesoscale spatio-temporal scales are 1 or 2 orders of magnitude smaller. The first observational campaigns targeting explicitly at the characteristics of STPPs were the Lateral Mixing experiment (LatMix) in the North Atlantic (Shcherbina et al., 2015) and the Submesoscale Experiments (SubEx) in the Southern California Bight (Ohlmann et al., 2017).

More detailed knowledge about the generation, kinematics, and dynamics of STPPs is conveyed by experiments with offline nested numerical models, so far predominantly applied to the regimes of eastern and western boundary currents. Using an idealised ROMS (Regional Ocean Modeling System, Shchepetkin and McWilliams (2005)) model with a flat bottom, a straight coast line, and uniform wind stress, Capet et al. (2008a, b, c) investigated the mesoscale to submesoscale transition in the California Current system. Based on 5 different model setups with variable horizontal resolution ranging from 12 to 0.75 km, they found that vigorous STPPs develop as the horizontal grid scale was reduced to $\mathcal{O}(1)$ km. The STPPs are initialised by the

generation of submesoscale fronts that are strained between mesoscale eddies. Some of these fronts become unstable, develop submesoscale meanders, and fragment into roll-up vortices. These processes are accompanied by vertical velocities up to 50 m day⁻¹ and by relative vorticity values of $\mathcal{O}(f)$, where f is the Coriolis parameter. Computations of the energy balance showed that significant conversion from potential to kinetic energy (baroclinic instability) takes place, both in the mesoscale and submesoscale waveband. A significant forward energy cascade occurs in the submesoscale range in transit to dissipation at the microscale. Using ROMS at very high horizontal resolution (150 m) and with realistic topography, Gula et al. (2016a) studied the submesoscale structure in the interior of a mesoscale cyclonic eddy that was generated on the inshore side of the Gulf Stream interacting with the shelf slope. The model results revealed multiple submesoscale fronts at the rim of the eddy that appear as elongated vorticity filaments, reaching locally multiple of f . Like in the California Current System, these filaments become unstable and break up into strings of submesoscale vortices that are advected into the interior of the mesoscale eddy. There, the cyclonic vortices are associated with low-salinity patches, indicating upwelling. Furthermore, it was shown that the divergence of the flow is dominated by intense small-scale patterns. These patterns are partially associated with the genesis of multiple fronts, but exhibit also characteristics of internal gravity waves propagating away from mesoscale fronts. In another article, Gula et al. (2014) investigated the life cycle of a submesoscale cold filament on the South Wall of the Gulf Stream: the formation of the filament (filamentogenesis) is primarily caused by an intensification of surface buoyancy gradients due to horizontal straining flows and a two-celled ageostrophic secondary circulation with strong surface convergence and associated downwelling in the centre.

The theory of frontogenesis and the associated secondary circulation is significantly shaped by the meteorological literature (e.g. Eliassen (1962)) where a front is formed in the confluence zone of a deformation field (Fig. 9.1b in Holton (1982)), that is generated in the centre of two crosswise arranged pairs of cyclonic and anticyclonic eddies. Typical characteristics of such a front are an along-front geostrophic jet and a cross-front ageostrophic overturning cell with downwelling on the dense side and upwelling on the less dense side of the front. For mesoscale fronts, this picture was authenticated by the idealised model studies of Bleck et al. (1988), Nagai et al. (2006), and Thompson (2000). For submesoscale fronts, the very recent model study of McWilliams (2017) confirms that “These circulation patterns, ..., are qualitatively similar to those due to the ‘classical’ mechanism of strain-induced frontogenesis”.

Baroclinic instability and instabilities driven by the horizontal shear of currents are the main processes leading to the instability of submesoscale fronts. The solutions of the classical problem of baroclinic instability (Charney, 1947; Eady, 1949) sufficiently explain the most unstable wavelength and growth rate of mesoscale disturbances, but these disturbances encompass a large fraction of the water depth including the surface layer and main thermocline. By contrast, another short-wave type of baroclinic instability was described by Blumen (1979) in the case of reduced stratification of the (atmospheric) boundary layer. The oceanic equivalents for this type are inertial (or centrifugal), symmetric, and mixed-layer instability. The latter was thoroughly investigated by Boccaletti et al. (2007) who showed that this class of instabilities may occur in the surface and bottom mixed layer; therefore, it is denoted as “mixed-layer instability”. It is a hybrid instability composed of gravitational and baroclinic instabilities finally leading to a flattening of isopycnals, and a positive (upward) buoyancy flux. It requires lateral buoyancy gradients, and it is composed of short modes between 200 m and 20 km and growth rates around 1 day⁻¹. The start-

ing point for such instabilities is the slumping of isopycnals that is constrained by rotation, because the thermal wind balance is established after a pendulum day. Thereafter, baroclinic instability generates wavelike disturbances that upset the thermal wind balance. As shown by Fox-Kemper and Ferrari (2008), the positive vertical buoyancy flux associated with mixed-layer instability is most important for the restratification of the upper ocean. By contrast, inertial (or centrifugal) instability does not require lateral buoyancy gradients but horizontal shear plus negative absolute vorticity. Therefore, inertial instability is driven by barotropic instability while a vertical buoyancy flux is not necessary. Pure inertial instability is unlikely to occur in the surface mixed layer, but it may arise when currents interact with topography on their right hand side (on the northern hemisphere), creating strong anticyclonic relative vorticity. A necessary condition for the occurrence of inertial instability is a relative vorticity smaller than $-f$ (Haine and Marshall, 1998; Thomas et al., 2013). Symmetric instability is a hybrid gravitational-inertial instability, and may be considered to be a special type of mixed-layer instability. To a first approximation, it arises when the potential vorticity is negative and the Richardson number is $Ri < 1$ (Boccaletti et al., 2007). The numerical simulations of Haine and Marshall (1998) confirm that symmetric instability dies as soon as $Ri > 1$ and baroclinic instability takes over. The transition from gravitational-inertial to gravitational-baroclinic instability was explored by Stamper and Taylor (2017) in detail. More in-depth conditions for symmetric instability were formulated by Taylor and Ferrari (2009) and Thomas et al. (2013).

Most of the numerical studies cited above manifest that STPPs act as a conveyor for kinetic energy from the mesoscale to the microscale. Besides this role, STPPs are also relevant for primary production (Mahadevan, 2016). In particular, the associated strong upward vertical motions transport nutrients into the sunlit ocean where plankton growth occurs, while carbon fixed by the phytoplankton cells is removed from the euphotic layer by downwelling events (Lévy et al., 2012).

In order to reproduce a realistic mesoscale physical environment, a ROMS model with 500-m horizontal resolution (referred to as R500 in the following) and realistic atmospheric forcing is nested into an operational model, the output of which is provided by CMEMS (Copernicus Marine Environment Monitoring Service, see below). An even finer nested ROMS model with a grid size of 100 m (R100) is used to enable the generation of STPPs, thus providing a base for an analysis of their properties and dynamics (Fig. 1).

The utilised numerical models are described in Section 2. The results of the numerical experiments are presented in Sections 3 and 4 and compared with observations in Section 5, followed by the conclusions. In the following, all time specifications refer to the year 2016 (unless stated otherwise) and are given in UTC (Universal Time Coordinated).

2 The models

2.1 Geographic and oceanographic setting

The Baltic Sea is a semi-enclosed marginal shelf sea with a mean water depth of 55 m and with narrow shallow connections to the North Sea. Due to river runoff, the water balance is positive driving an estuarine circulation with quasi-permanent outflow of fresh surface waters and an intermittent inflow of salty water from the North Sea. At the surface, this creates a horizontal salinity gradient with high salinities in the west and almost freshwater conditions in the far north. Salinity is increasing with

depth thus stratifying the water column year-round and generating a permanent halocline at about 60-m depth in the deeper basins. For more details see Feistel et al. (2008), Leppäranta and Myrberg (2009), or Osinski et al. (2010).

The area of this model study is separated into two basins, the Arkona Basin and the Bornholm Basin (Fig. 1). The Arkona Basin is the smaller one with a maximum water depth of 51 m, while the maximum depth of the Bornholm Basin is 92 m. The basins are connected by two channels, with an exchange of water limited by sills of 45 m depth in the Bornholmsgat (Magaard and Rheinheimer, 1974) and 31 m between Rönnebank and the island of Rügen.

2.2 The CMEMS product

The CMEMS product is provided at <http://marine.copernicus.eu>, product BALTICSEA_ANALYSIS_FORECAST_PHY_003_006, ~~issue 1.8, last access 1 November 2019~~ [last access 17 Februar 2020](#) since April 2015, ~~comprising 2015~~. The product is based on HBM (HIROMB-BOOS model (Berg, 2012)), which is an operational ocean circulation model predicting the physical conditions of the Baltic Sea. It is referred to as CMEMS-HBM in the following. CMEMS-HBM used in this study is documented in the Product User Manual CMEMS-BAL-PUM-003-006.pdf, Version 2.1, and the validation framework is described in the Quality Information Document CMEMS-BAL-QUID-003-006.pdf. HBM is running twice daily at DMI (Danish Meteorological Institute) in Denmark, and a backup production system is running at BSH (Bundesamt für Seeschifffahrt und Hydrography) in Germany. While the DMI setup uses meteorological data from DMI-HIRLAM with a horizontal resolution of 5 km, the BSH version is driven by data from the Cosmo-EU model with 7-km horizontal resolution provided by the German Weather Service, DWD. CMEMS-HBM comprises daily mean and hourly instantaneous fields at a horizontal resolution of 1 nmi (nautical mile) at 25 depth levels spaced at 5 m between the sea surface and 100-m depth, and additional levels below at 150, 200, 300, and 400-m depth. For this article, the daily mean fields of June 2016 were utilised that contained 30 records of the prognostic variables potential temperature, salinity, horizontal velocity, and sea surface height for each June day. ~~The product is based on HBM (HIROMB-BOOS model (Berg, 2012)), which is an operational ocean circulation model predicting the physical conditions of the Baltic Sea at higher vertical resolution. Therefore, it is referred to as CMEMS-HBM in-~~ [The modeling activity for this study started in early 2017. At that time, the following CMEMS-HBM reanalysis product, BALTICSEA_REANALYSIS_PHY_003_011 \(also available at <http://marine.copernicus.eu>\), was not yet available since it was released for the first time in April 2018. Hence, there was no alternative or CMEMS-HBM at the required horizontal resolution.](#)

2.3 ROMS

The employed numerical ocean circulation model ROMS is a hydrostatic, free-surface, primitive equations model. Its algorithms are described in detail in Shchepetkin and McWilliams (2005). In the vertical, the primitive equations are discretised over a variable topography using stretched terrain-following coordinates, so-called s-coordinates (Song and Haidvogel, 1994). In the horizontal, spherical coordinates are used. Biharmonic mixing along isopycnic surfaces is applied to the tracers, both in R500 and R100, while biharmonic mixing of momentum is used in R500 and a monoharmonic formulation in R100. The vertical mixing of momentum and tracers is parameterised with the GLS (Generic Length Scale) scheme by Umlauf and Burchard (2003) in R500, and with the interior closure by Large et al. (1994) in R100, referred to as the KPP scheme. For the bottom

friction, a quadratic law is applied, and the pressure gradient term is computed using the standard density Jacobian algorithm by Shchepetkin and Williams (2001). The air-sea interaction boundary layer in ROMS is formulated by means of the bulk parameterisation by Fairall et al. (1996). R500 and R100 have the parameters and equations listed in Table 1 in common, while the individual grid-size-dependent parameters and properties are summarised in Table 2. As the spatial scales of the smallest known STPPs are $\mathcal{O}(10\text{ m})$, it is expected that large and medium-scale STPPs are resolved.

2.4 Nesting, boundary conditions

There are two offline nesting steps: R500 is nested in CMEMS-HBM, and R100 is nested in R500. While the ROMS-to-ROMS nesting is technically straightforward, the first nest is somewhat more delicate, because the CMEMS-HBM output is provided on depth levels while ROMS uses s-coordinates. ~~In addition, the bathymetry of CMEMS-HBM is not contained in the output provided by CMEMS.~~ Therefore, the setup of the R500 domain and the nesting was accomplished as follows:

1. The bathymetry of the GEBCO_2014 grid (General Bathymetric Chart of the Oceans, 30 arc seconds horizontal resolution) was used as the lower boundary of the R500 domain, and it was smoothed iteratively until the stability condition $rx_0 \leq 0.2$ was reached everywhere (see Haidvogel et al. (2000) and Table 2).
2. The CMEMS-HBM prognostic variables were interpolated linearly onto the R500 horizontal grid at each CMEMS-HBM depth level in 24-hour intervals and for each day of June.
3. The R500 vertical grid was defined according to Table 1 and the CMEMS-HBM fields were interpolated vertically onto the R500 vertical grid. The first record of the resulting data set served as initial condition for the R500 integration, while the lateral boundary conditions were extracted from all records.
4. R500 was integrated for one day, and the near bottom velocities were checked for odd features that might have been caused by ~~improper alignment of the R500 bathymetry with the unknown~~ non-zero normal velocities at topographic obstacles which were not resolved in CMEMS-HBM ~~bathymetry~~. If such features (e.g. abnormal vertical motions) were noticed, the R500 bathymetry was manually adjusted and the above procedure was iteratively repeated, starting with step 3.

For the R500-to-R100 nesting, the same vertical grid definition was used, and no interpolation from depth levels to s-coordinates was required. Special care was taken for the preparation of the initial and boundary conditions, as a nesting ratio of 5 is rather challenging: cubic splines were used for the horizontal interpolation of the prognostic variables of R500 onto the child's grid, because the structures of jet flows across the open boundaries of the R100 domain looked more realistic than those obtained by linear interpolation. In addition, the downscaled fields were generated in 3-hour intervals, leading to a smoother temporal change of the lateral boundary conditions. Cubic splines were used as well for the interpolation of the atmospheric forcing fields on the R100 grid. Because in a nested configuration the s-coordinates of the parent and the child at any location are only identical if the bathymetry is the same, the bathymetry of R100 was cloned from R500 and linearly interpolated onto the finer grid.

For each nest, radiation boundary conditions with nudging (Marchesiello et al., 2001) were applied to temperature and salinity, barotropic and baroclinic momentum, and the mixing of turbulent kinetic energy along the lateral boundaries. The boundary conditions of the free surface were defined according to Chapman (1985). In all ROMS setups, the nudging time scales were set to 2 days for the corresponding variables. At the surface, the air-sea interaction in the ROMS nests was specified by means of atmospheric forcing fields from the so-called “assimilation runs” of the ICON-EU model, provided by the German Weather Service (DWD). The output of these runs was considered to be the best available product, because the runs were initialised in 3-hour intervals at 00 h, 03 h, 06 h, . . . and driven by the most recent near-real time assimilation fields, in contrast to the forecast runs initialised semidaily at 00 and 12. The horizontal resolution of ICON-EU is about 6.5 km and output is produced in 1-hour intervals.

10 3 R500: model results and validation

STPPs are generated in the straining field of mesoscale eddies. According to Osinski et al. (2010), the condition for eddy resolving models of the southern Baltic is that the Rossby radius is resolved by at least 4–5 horizontal nodes. As the Rossby radii in the Bornholm and Arkona Basins are in summer around 7.2 and 3.7 km, respectively (Fennel et al., 1991), and since the grid size of CMEMS-HBM is 1 nmi, it is definitively not eddy-resolving or even eddy-permitting (2–3 nodes) in the Arkona Basin and perhaps eddy-permitting at best in the Bornholm Basin. The eddy-resolving R500 was initialised from CMEMS-HBM on 1 June 00:00 and integrated for 30 days. The vertical mixing in R500 is accomplished with GLS using the $k - \omega$ setup of Wilcox (1988) with the stability function of Kantha and Clayson (1994).

For a Lagrangian water parcel, the freshwater budget is controlled by $P - E$ which is the difference between precipitation P and evaporation E . On the longterm average, $P - E$ is around ~~32 mm year⁻¹ (Smedman et al., 2005) or equivalently~~ 0.1 mm day⁻¹. ~~Hence, the budget is almost zero and the residual may lead to~~ (Smedman et al., 2005) that may cause maximum salinity changes on the order of 10^{-2} per month for typical mixed-layer depths of 10 m (see Section 4.4.3). In contrast, the heat budget is dominated by the short wave radiation flux leading to warming around 5° C of the near surface layers in June. Hence, salinity is the ideal parameter to trace turbulent patterns as in the Baltic Sea it behaves like a passive and quasi-conservative tracer. Fig. 2 shows salinity in the uppermost layer of CMEMS-HBM and R500 on 1, 10, 20, and 30 June (left and centre panels). R500 rapidly develops turbulent structures that are only marginally identifiable in CMEMS-HBM. These are, for example, the low-salinity outbreaks along the northern boundary, a high-salinity eddy in the Arkona Basin, and mushroom-like patterns east and southeast of Bornholm on 10 and 20 June. The horizontal scales of these features are $\mathcal{O}(10 \text{ nmi})$, but also smaller patterns with a horizontal extent of 5 nmi, or even less, are generated by R500, such as the filaments around Bornholm and the meanders immediately off the Polish coast on 20 June. Hence, R500 apparently bridges the gap between the mesoscale and the submesoscale.

R500 provides the initial and boundary conditions for R100. Insofar, it is worth knowing to what extent its generated two-dimensional turbulence is in a state of statistical equilibrium, and at what time during the integration an equilibrium state is attained. To determine this so-called spin-up time, the blue dash-dotted graph in Fig. 3 shows a time series of the domain-

averaged kinetic energy per unit mass, KE_{R500} ; it fluctuates strongly between 3×10^{-3} and more than $12 \times 10^{-3} \text{ m}^2 \text{ s}^{-2}$ and does not reach a stable value. Evidently, it is difficult to determine the spin-up time from R500 because KE_{R500} is strongly impacted by wind bursts as shown by the black curve. Therefore, R500 was compared to a run where the atmospheric forcing was completely turned off by setting the air-sea fluxes of net heat, fresh water and momentum to zero. This run is referred to as R500_NF (“No Forcing”). Here, the intense fluctuations of KE vanished as shown by KE_{R500_NF} (blue solid graph), but there are still some smaller-scale oscillations with maxima on 11, 14, 20, and 28 June, the existence of which impede the estimate of a spin-up time. These oscillations are slightly correlated with the wind bursts lagging behind for about one day. Potentially, they are triggered by the remote forcing of CMEMS-HBM via the lateral boundaries which explains the time lag. Another cause could be vacillations of KE which is a well-known peculiarity of nonlinear rotating fluids (Hide, 1958; Fröh, 2015). In order to filter out the oscillations, the cumulative average $\overline{KE_{R500_NF}}$ was computed. This quantity is frequently used in time series analysis in order to determine the time scale at which a stochastic time series reaches stationarity. In the actual case, $\overline{KE_{R500_NF}}$ attains a maximum of 6×10^{-3} on 1 June and then decreases to about $3.4 \times 10^{-3} \text{ m}^2 \text{ s}^{-2}$ on 7 June. Thereafter, it increases steadily to 4.4×10^{-3} on 22 June and remains constant until the end of the month. Hence, stationarity is reached after about 22 days, corresponding to an e-folding scale of 12 days that may be considered as the spin-up time.

The analysis of the prognostic fields of R500_NF yielded an additional perception: the tracer fields exhibit much more spatial variability in comparison to the corresponding fields of R500 (see the right panel in Fig. 2). A rich variety of smaller details is revealed that were hidden in the forced run, such as the STPPs along the German and Polish coast, multiple filaments in the entire model domain, and sharper frontal gradients. On longer time scales, the larger scale patterns also develop differently. Similar findings were presented by the observational study of Kubryakov and Stanichny (2015): from an analysis of satellite altimeter data, they demonstrated that a weakening of the large-scale circulation leads to baroclinic instability of the Rim Current in the Black Sea. An explanation for this behaviour was provided by the earlier studies of Zatsepin et al. (2005). Literally, their laboratory experiments showed that “The development of an instability, the generation of meanders, and the formation of eddies are prevented by the Ekman divergent circulation caused by the wind, which presses the frontal current to the coast throughout the periphery of the tank, thus contributing to the significant increase in kinetic and available potential energy. When the wind forcing stops, the instability grows rapidly.” While the above mentioned papers focused on mesoscale instabilities, Renault et al. (2018) showed that the evolution of submesoscale instabilities in the Californian Upwelling System is damped by the wind stress as well. Another reason for the decrease of submesoscale activity in response to the increase of the wind speed was provided by Mahadevan et al. (2010), who showed that the wind field blurs the small-scale features by horizontal mixing. These findings are important because they guide the setup of the R100 experiments below.

A comparison with observations is shown in Fig. 4 by means of the surface salinity from R500 and a RGB composite derived from a satellite-borne multi-spectral image in the visible spectral range. In the latter, the patterns arise due to the presence of naturally occurring optically active substances like chlorophyll. The comparison between these different quantities is legitimate because both act like passive flow tracers. The image reveals three spiral-like patterns that may be considered as proxies for cyclonic (C1, C2) and anticyclonic (AC) eddies. The centre of C1 is almost at exactly the same location [$15^\circ 30'$ E, $54^\circ 40'$ N] in the satellite image and in R500. The centre of C2 is at about [$14^\circ 10'$ E, $55^\circ 7'$ N] in R500. Unfortunately, the central part

of this cyclone is masked by clouds in the satellite image, but the unmasked portions provide evidence for its real existence. Strong peripheral fronts are visible both in R500 and the satellite images. The positions of AC differ the most: in Fig. 4b, the centre of that anticyclone is at [15°50' E, 54°57' N], in Fig. 4a at about [15°40' E, 55°0' N], hence roughly 7 nmi to the west. It is legitimate to associate these positions with each other because both in R500 and in the satellite snapshot, as AC is the anticyclonic “partner” of C1, both form a mushroom-like eddy pair. On the whole, the apparent similarities between the observations and the R500 simulations builds some confidence that R500 produces realistic results. Moreover, the above mentioned eddies and fronts are already visible on 20 June in R500 (see Fig. 2) but not at all in CMEMS-HBM at the same time. Hence, in R500 the mesoscale environment is apparently better reproduced than in CMEMS-HBM.

4 R100: results

Apparently, R500 is able to reproduce STPPs but only those in the low-wavenumber part of the spectrum. To provide more insight into the higher-wavenumber parts, R100 was initialised from R500 on 15 June 00:00 and integrated until 29 June 00:00. Based on the experience with R500, the surface fluxes in R100 were turned off. This is indeed a strong simplification and the model results may differ significantly from the reality. However, it helps to understand the evolution and the dynamics of submesoscale processes, which are controlled primarily by potential vorticity conservation in the adiabatic limit (McWilliams, 2008). Different formulations and coefficients for the horizontal eddy viscosity and diffusivity were tested. The best results were obtained from a model run with mono-harmonic mixing for the momentum and biharmonic mixing for the tracers (Table 2). This choice caused a minimum damping of STPPs, and a better representation of small-scale details without numerical noise. Moreover, ~~as R100 is rather expensive in terms of computer resources,~~ the vertical mixing was parameterised with KPP instead of the time-consuming GLS scheme. From a KE analysis, the spin-up time was an estimated 2 days. Hence, a 6-day spin-up period starting on 15 June was sufficient to produce statistically equilibrated fields on 20 June and thereafter.

In the following, the results of R100 are illustrated by Figs. 5 – 17, and 18b, c. All figures are snapshots taken at the specified day at 00:00.

4.1 Tracer patterns

The top-layer patterns of salinity and potential temperature are shown in the left and centre panels of Fig. 5 in 3-day intervals 20–29 June, where the top layer ranges between about 0.3 and 1.7 m. To asses the effect of the downscaling, the salinity patterns are compared with the corresponding ones of R500_NF on 20 and 30 June (Fig. 2). The large-scale features resemble each other to a high degree, such as the low salinity to the west and the east of Bornholm and the higher-salinity pool south of the island. However, R100 exhibits much more variability in the submesoscale waveband and STPPs down to 1-km scales are resolved. The signatures of such small-scale features are better visible in the temperature patterns, such as the cold patches in the southern region of the R100 domain.

The knowledge of the temporal change of the density (or buoyancy) gradient is essential for frontogenetic and frontolytic processes and filamentogenesis, that is expressed by the frontal tendency equation (Holton, 1982; Capet et al., 2008b; Gula et

al., 2014). As a first approach, the absolute horizontal gradient of potential density, ρ ,

$$|\nabla\rho| = \sqrt{\left(\frac{\partial\rho}{\partial x}\right)^2 + \left(\frac{\partial\rho}{\partial y}\right)^2} \quad (1)$$

is calculated, where x and y are the Cartesian coordinates pointing to the east and to the north, respectively. This quantity is shown in the right column of Fig. 5. Narrow filaments indicate locations of intensified gradients, i.e. density fronts. From the sequence of the images, it appears that the quantity of the fronts increases with time and that the gradients amplify. This is partly confirmed by a frequency distribution of $|\nabla\rho|$, shown in Fig. 6a: from 15 to 25 June, the frequency of occurrence grows consistently in all $|\nabla\rho|$ intervals. From 25 to 29 June, however, this behaviour changes. While the frequency distribution for $|\nabla\rho| < 1.2 \times 10^{-3} \text{ kg m}^{-4}$ remains almost the same, it decays at the same time for larger values of $|\nabla\rho|$. Hence, there are less locations with strong gradients indicating a weakening of strong density fronts. In order to determine whether there is an upper limit for the growth of $|\nabla\rho|$, R100 was repeated but now the initial and open boundary conditions were taken from R500_NF. The resulting frequency distribution (Fig. 6b) exhibits more occurrences of strong gradients than in panel a on 15 and 20 June. This is plausible, because the atmospheric forcing in R500 has blurred the gradients. The frequency distribution of 25 June is almost identical to that of 20 June, and from 25 to 29 June it decays in the same way as in panel a. Hence, a “frontal arrest” occurs apparently when the strongest gradients approach a critical value around $3 \times 10^{-3} \text{ kg m}^{-4}$ that is reached on 25 June in panel a and already on 20 June in panel b. However, it is not clear whether physical processes or numerical diffusion (or both) limit the increase of gradients. For the physical processes, \mathbf{Q}_w , the straining deformation by the vertical velocity (see eq. (7) below), would be a suitable candidate, because downwelling on the dense side of a front and upwelling on the less dense side lead to a weakening of the cross-front density contrast. Another process was identified by Sullivan and McWilliams (2018) and Gula et al. (2014), who investigated the life cycle of a dense filament. There, frontogenesis is arrested at a small width of about 100 m. It is mostly driven by an enhancement of turbulence through submesoscale horizontal shear instabilities that draw their energy primarily from the horizontal mean shear via the horizontal Reynolds stresses.

4.2 Kinematics

Fig. 7 shows the near-surface properties of the velocity field and derived quantities on 26 June. This day was chosen because it represents the conditions in the middle of the survey period and it allows comparisons with Fig. 5.

4.2.1 Horizontal currents

The horizontal velocity field (Fig. 7a) is separated into two regimes: high current speeds frequently exceeding 0.1 m s^{-1} are found north of about $54^\circ 50'$ N, south of $54^\circ 35'$ N, and west of $14^\circ 40'$ E. They are organised in jet-like streaks or circular features, and their positions are clearly related to the main density fronts shown in Fig. 5. Maximum speeds of 0.32 m s^{-1} are found in the anticyclonic eddy southeast of Bornholm. The high-speed regime surrounds a pool of water with speeds lower than 0.1 m s^{-1} in the centre of the model domain. The transition between the high-speed and low-speed regimes appears to be related to the 40-m depth contour (the white line in Fig. 7a), at least in the south and west. Potentially, the bathymetry is acting

as a waveguide for the westward jet south of Bornholm. One may note that both the anticyclone AC and the cyclonic eddy C1 are at about the same position as in Fig. 4a three days before.

4.2.2 Relative vorticity

Information about the dynamical properties of the flow field is derived from the relative vorticity ζ , i.e. the vertical component of the curl of the total velocity:

$$\zeta = (\nabla \times \mathbf{V})_z = \frac{\partial v}{\partial x} - \frac{\partial u}{\partial y} \quad . \quad (2)$$

Here, z is the vertical coordinate and u, v, w are the zonal, meridional, and vertical components of the total velocity vector \mathbf{V} . Fig. 7b reveals the whole range of relative vorticity (scaled by f) between the largest scales of about 20 km and the smallest scales on the order of the grid size of 100 m. The dominant mesoscale patterns are the large anticyclonic relative vorticity patch southeast of Bornholm and the wavelike structures to the south that belong to the westward jet mentioned above. Further west and south in the shallow water, pools of concentrated cyclonic relative vorticity vary mostly between 5 and <1 km in size. The smallest visible features are cyclonic streamers, with width approaching the Nyquist scale of 200 m.

There is a strong asymmetry between the distributions of cyclonic and anticyclonic relative vorticity. The cyclonic relative vorticity is organised in thin filaments, comma-like “hooks”, and quasi-circular pools of water. In contrast, the distribution of the anticyclonic relative vorticity is smoother, and the occupied area is larger than the area utilised by $\zeta/f > 0$, which is in agreement with McWilliams (2016). The frequency distribution shows that $\zeta/f < 0$ in 63 % of the grid cells, while positive values are found only in 37 %. Moreover, in less than 0.2 % of the grid cells, $\zeta/f < -1$, indicating negative potential vorticity (Dewar et al., 2015; Gula et al., 2016b) and associated inertial instability.

The relative vorticity structures north of 55° N exhibit lamellar patterns that are probably caused by false advection from the parent domain, although cubic splines were applied to all prognostic variables in the context of the downscaling. Such patterns are only visible in the relative vorticity patterns, while the horizontal velocities (Fig. 7a), and the tracer fields (Fig. 5) look rather reliable. Obviously, the downscaling did a good job with the prognostic variables, but along the open boundaries it may not have been able to reflect the first derivatives correctly.

4.2.3 Divergence and vertical motion, impact of bathymetry

The horizontal divergence of the velocity,

$$\delta = (\nabla \cdot \mathbf{V})_h = \frac{\partial u}{\partial x} + \frac{\partial v}{\partial y} \quad , \quad (3)$$

is displayed in Fig. 7c. It can be divided into 3 different classes of textures: Class I structures are thin, less than 1-km wide filaments of negative divergence (convergent flow) that are bordered by wider areas of divergent flow on one or both sides. The major density fronts (Fig. 8) are aligned with such filaments. On the contrary, the areas of convergent flow that are not congruent with enhanced horizontal density gradients belong to Class II. In particular, those patterns tagged by the yellow arrows in Fig. 8 are not correlated with enhanced density gradients (note that the value of the magenta contour refers already to

rather low gradients, cf. Fig. 5). It is conjectured that these features are related to internal waves generated during the genesis of nearby fronts and jets (Plougonven and Snyder, 2007; Shakespeare and Taylor, 2014; Shakespeare, 2019). This is confirmed by Fig. 9: the vertical displacements of isopycnals between $15^{\circ}07' \text{ E}$ and $15^{\circ}09' \text{ E}$ are clear indicators for internal waves with a wavelength around 1000 m. In order to verify that these patterns are caused by internal waves, their frequency at 10-m depth was estimated to about $4 \times 10^{-4} \text{ s}^{-1}$, somewhat less than the buoyancy frequency at the same depth ($\approx 5 \times 10^{-4} \text{ s}^{-1}$) but larger than the Coriolis frequency. Hence, the patterns are indeed intermediate-frequency internal waves. However, a closer inspection is not advisable, because ROMS is hydrostatic and various properties of internal waves are correctly reproduced only in nonhydrostatic models (Wadzik and Hodges, 2009; Vitousek and Fringer, 2011).

Class III textures are small patches of either sign and horizontal scales of $\mathcal{O}(1) \text{ km}$. They are found almost everywhere, but their highest values are found in the area of higher current speeds in the northwest corner of the domain and in the anticyclonic eddy southeast of Bornholm. The topography of potential density surfaces in the anticyclone shows that the patches are accompanied by large excursions of isopycnals, indicating intense internal wave activity. These waves are emitted from fronts at the periphery of the eddy, and the superposition of internal waves coming from different directions leads to the rugged shape of isopycnals and contemporaneously to the patchy pattern that is in agreement with the findings of Väli et al. (2018).

In ROMS, the vertical speed is computed from the continuity equation. As expected, the spatial patterns of the vertical speed are therefore identical with that of the divergence, but only for the divergence in the top layer and the vertical speed at the base of that layer. In contrast, the horizontal distribution of the vertical speed at 5-m depth (Fig. 7d) still resembles the top layer divergence, but with significant differences. The most striking discrepancy is that the thin filaments of convergent flow belonging to Class I (Fig. 7c) are not at all reflected by the vertical motion pattern. On the other hand, the vertical motions related to the internal wave packets discussed above are still clearly visible. To explain this disagreement, Fig. 9 shows a zonal section of the vertical speed, together with the potential density and the meridional velocity. The vertical motion induced by the internal waves attains speeds of up to $\pm 20 \text{ m day}^{-1}$ ($\approx 0.2 \text{ mm s}^{-1}$) and the signal is pronounced over the entire vertical range between the surface and 10-m depth; by contrast, the magnitude at the location of the front barely exceeds 5 m day^{-1} ($\approx 0.06 \text{ mm s}^{-1}$) and the vertical speed diminishes with increasing depth. Apparently, the major surplus (deficit) of mass created by the frontal convergence (divergence) at the surface, is discharged (imported) by the frontal jet or the secondary divergent circulation (cf. Fig. 1 in McWilliams et al. (2009), or Bleck et al. (1988)). As such a horizontal discharge/import mechanism is not available in a pure internal wave field, the only way to respond to any non-zero divergences is by vertical motion; this is explained in more detail in Section 4.4.4. In contrast to these rather moderate vertical velocities, extreme values around $\pm 250 \text{ m day}^{-1}$ (equivalent to $\approx 3 \text{ mm s}^{-1}$) are associated with the above mentioned Class III textures.

In Section 4.2.1, it was already mentioned that the horizontal current patterns are somehow correlated with the water depth. Such a relationship applies as well for the patterns of the other variables displayed in Fig. 7. ~~The, e.g. the~~ spatial variability of relative vorticity and the frequency of narrow filaments of confluent flow are clearly enhanced in the shallow water regions. ~~In contrast, the texture of the vertical speed is rather smooth there, indicating less internal wave activity~~ An explanation for this different behaviour is given by McWilliams (2019) who identified two principal mechanisms for the generation of STPPs:

(i) extraction of available potential energy due to horizontal gradients in the weakly stratified surface layer (mixed-layer instability), and (ii) topographic-drag vorticity generation in flows along a sloping bottom, followed by boundary current separation and wake instability. As strong bottom slopes are found only along Rönnebank and in the south of the R100 domain (see Fig. 1), the mechanism (ii) is obviously significant in those areas. However, for water depths > 50 m, the bottom is mostly flat and topographic-drag vorticity generation can be excluded.

4.3 Impact of atmospheric forcing

In order to justify the approach to run R100 without atmospheric forcing, R100 was repeated but now including all fluxes at the air-sea interface as provided by the ICON-EU model. The results for 26 June of the same parameters as in Fig. 7 are displayed in Fig. 10.

- 10 The patterns of the horizontal velocity (Figs. 7a and Fig. 10a) resemble each other but only in the “high-velocity regimes” west and east of Bornholm. Here, the direction of the currents did not change significantly but the maximum speeds increased from 0.32 to about 0.42 ms⁻¹. In contrast, the pattern in the low-speed pool in the centre of the model domain changed dramatically. While there in the no-forcing run the maximum speeds rarely exceeded 0.1 ms⁻¹, the highest speeds are now about twice as high. Moreover, the wind stress caused a unidirectional flow to the east as opposed to alternating flow directions in Fig. 7a. The atmospheric forcing impacts severely the top-layer relative vorticity patterns (panels b of the respective figures). Submesoscale features are no more detectable, i.e. there are no filaments, comma-like “hooks”, and circular pools of cyclonic vorticity. However, some mesoscale structures are still visible, for instance the large anticyclonic eddy southeast of Bornholm and the small cyclone close to the eastern boundary at about 54°45' N. Overall, the atmospheric forcing acts like a filter that wiped out any structures with scales of less than about 10 km. This smoothing effect also removed the Class I divergence patterns (panels c). In contrast, the number of small-scale patches (Class III) and their amplitude has increased. This is also reflected by the vertical velocity (panels d). Presumably, the imposed momentum stress enhanced the internal wave activity.

- 25 In summary, not before the atmospheric forcing is switched off, STTPs start to grow. This reflects a situation which also occurs in Nature when the wind subsides. For instance, applying a high-resolution Princeton Ocean model to the Gulf of Finland, Zhurbas et al. (2008) and Väli et al. (2017) demonstrated that the horizontal eddy viscosity increased and submesoscale cyclonic vortices evolved as soon as the wind slackened.

4.4 Fronts and eddies

4.4.1 Frontogenesis and eddy formation

- 30 The right column of Fig. 5 shows snapshots of $|\nabla\rho|$. A statistical analysis indicates an increase of the frequency of occurrence of high density gradients and a general sharpening of the density fronts with time. However, the latter provides only a statistical information and it does not show the locations where the fronts are sharpening (frontogenesis) or weakening (frontolysis) and which physical processes are contributing thereto. The missing information is conveyed by the frontal tendency equation

$$F = \frac{d}{dt} |\nabla\rho|^2 \quad , \quad (4)$$

which was introduced by Hoskins (1982) into the meteorological literature. F describes whether the absolute horizontal density gradient of a Lagrangian water parcel is growing ($F > 0$) or weakening ($F < 0$) with time t . Using the nomenclature of Capet et al. (2008b), F is further decomposed as

$$F = (\mathbf{Q}_h + \mathbf{Q}_w + \mathbf{Q}_{dv} + \mathbf{Q}_{dh}) \cdot \nabla \rho \quad . \quad (5)$$

5 Here, the terms are defined as

$$\mathbf{Q}_h = - \left(\frac{\partial u}{\partial x} \frac{\partial \rho}{\partial x} + \frac{\partial v}{\partial x} \frac{\partial \rho}{\partial y}, \frac{\partial u}{\partial y} \frac{\partial \rho}{\partial x} + \frac{\partial v}{\partial y} \frac{\partial \rho}{\partial y} \right), \quad (6)$$

which is the vector representing the straining deformation by the horizontal total velocity. The vector may be separated into contributions \mathbf{Q}_{geo} from the geostrophic and \mathbf{Q}_{ageo} from the ageostrophic velocity, respectively.

$$\mathbf{Q}_w = - \frac{\partial \rho}{\partial z} \left(\frac{\partial w}{\partial x}, \frac{\partial w}{\partial y} \right) \quad (7)$$

10 is the equivalent quantity for the vertical velocity, and

$$\mathbf{Q}_{dv} = \left(\frac{\partial \rho}{\partial z} \frac{\partial^2 A_V^\rho}{\partial x \partial z} + \frac{\partial A_V^\rho}{\partial z} \frac{\partial^2 \rho}{\partial x \partial z}, \frac{\partial \rho}{\partial z} \frac{\partial^2 A_V^\rho}{\partial y \partial z} + \frac{\partial A_V^\rho}{\partial z} \frac{\partial^2 \rho}{\partial y \partial z} \right) \quad (8)$$

is the contribution from vertical mixing where $A_V^\rho = A_V^\rho(x, y, z, t)$ is the eddy diffusion coefficient for density. Finally,

$$\mathbf{Q}_{dh} = \left(\frac{\partial D}{\partial x}, \frac{\partial D}{\partial y} \right) \quad (9)$$

is the effect of the horizontal diffusion of density, D .

15 The components of the tendency equation are displayed in Fig. 11 for a subregion of the R100 domain. The quantities F , Q_{geo} , Q_{ageo} , Q_w , Q_{dv} , and Q_{dh} at 2-m depth are shown in the centre and bottom rows. They are the scalar products of the corresponding vectorial quantities \mathbf{Q} and $\nabla \rho$. For comparison with the dynamical background, the top-layer patterns of $|\nabla \rho|$, ζ/f , and the vertical velocity w at the base of the top layer are displayed in the top row of the same figure. The subplots of $|\nabla \rho|$ and ζ/f reveal four major frontal systems, F1–F4, and two cyclonic vortices, C3 and C4. The width of all fronts and the
20 radius of the circular cyclone C3 (defined by the zero-crossings of ζ/f) is ≤ 2 km, while the semi-axes of the elliptical-shaped cyclone C4 vary between 2 and about 4 km. Both frontogenetic and frontolytic processes are roughly evenly distributed and of the same order of magnitude for F , Q_{geo} , and Q_w . This is different for Q_{ageo} and Q_{dv} which are primarily frontogenetic. Moreover, Q_{dv} only differs significantly from zero at the fronts, while at the positions of C3 and C4, it is close to zero. By contrast, the contribution of Q_{dh} to the tendency F is everywhere negligible. F exhibits a bimodal pattern for F1 and F2, with
25 $F < 0$ on the anticyclonically sheared side and $F > 0$ on the cyclonic side. A comparison of the patterns of the components of F reveals that $F > 0$ in F1 and in the western and central parts of F2 is predominantly supported by Q_{ageo} and Q_{dv} and to a lesser extent by Q_{geo} , while the sign of Q_w is alternating along-front. On the other hand, $F < 0$ in those parts is primarily supported both by $Q_{geo} < 0$ and $Q_{dv} < 0$. A bimodal structure is also visible for F4. Here, frontogenesis is supported both by Q_{geo} and Q_{ageo} , and frontolysis only by Q_w . For F3, the situation is similar.

The above results conflict to those obtained by Capet et al. (2008b), referred to as CMMS in the following: according to their Fig. 7, the “residual” (equivalent to F in this paper) at the sea surface is generally negative and the geostrophic contribution is always positive, while the corresponding quantities in the current article exhibit a clear bimodal structure. On the other hand, the contributions from ageostrophic straining and vertical diffusion are bimodal in CMMS but Q_{ageo} and Q_{dv} are predominantly positive. Similarly, the impact from vertical straining in CMMS is everywhere negative, in contrast to Q_w that is bimodal as well and the sign is alternating along-front. The cause for these disagreements might be the different horizontal resolution of ROMS (750 m in CMMS and 100 m in R100). By contrast, the multimodal structures and the alternating along-front sign changes of F and its components resemble more those obtained by Gula et al. (2014).

Prominent structures of the tendency terms are also visible in C3 and C4, but those will be investigated in detail in a follow-up paper investigating the dynamics of a submesoscale cyclone.

4.4.2 Submesoscale upwelling in eddies

As noticed above, the vertical motion pattern in almost the entire model domain is impacted by internal waves that frequently blur the corresponding signals of fronts. However, in some settings, the vertical motion related to submesoscale fronts and eddies may supersede the internal wave-driven vertical velocity which can be seen in Fig. 7d. Such a situation is given during the life cycle of the submesoscale eddy C3 depicted in Fig. 11. C3 originates from a dense (cold and salty) streamer that invaded the area from the south, starting on 24 June around noon. While the streamer stretched farther to the north, it rolled up into C3 on 25 and 26 June (Fig. 12a–c; the entire process is shown in an animation on the web site https://www.hzg.de/institutes_platforms/coastal_research/operational_systems/coast_ocean_measurement/topics/index.php.de#tab-100, last access 1 March 2019). In Fig. 12d–f, the vertical speed at 5-m depth is shown for the same period of time. On 24 June before the winding-up of the eddy started, the vertical motion pattern is controlled by a train of internal waves travelling from northeast to southwest. One day later, the impact of the eddy formation on the vertical motion field becomes visible: two extended patches with vertical speeds of either sign are located south and north of the eddy core. On 26 June, the pronounced downwelling area is smaller but the upwelling still prevails at the same location. Apparently, the eddy-driven vertical motion supersedes the signal of the internal waves and causes persistent upwelling for a day or even more as can be seen in Fig. 12f: at the position of the crosshair, upwelling is still visible, although the eddy centre has moved already to the north by about 2 nmi.

4.4.3 Instability mechanisms

The results above impressively show that submesoscale eddies grow rapidly in the R100 domain, preferably in the shallow areas with water depths less than 40 m (Fig. 7). However, it is not yet clear if inertial, symmetric or mixed-layer instability drive the eddy growth. In the following, the R100 fields are analysed for criteria necessary for the occurrence of any type of these instabilities.

For inertial instability, negative absolute vorticity, ζ^a , is a necessary condition, which is equivalent to $\zeta^a = \zeta + f < 0$ or $\zeta/f < -1$. It can be seen in Fig. 7b (blue regions) that $\zeta/f < -1$ is satisfied along the coast of Bornholm and at a few isolated locations along the meridional open boundaries, i.e. close to the centre of the cyclonic eddy in the northwest corner and between

54°25' and 54°30' N at the eastern boundary. However, the latter appearances are ignored because they are potentially due to false advection effects of relative vorticity discussed above. A zoomed image of ζ^a/f in the surface layer of R100 (Fig. 13) shows that negative values are found at 7 locations around Bornholm, indicating the birthplaces of disturbances driven by inertial instability. All of them are directly attached to the coast, but favourable conditions for the growth of the disturbances seem to prevail only at sites no. 2 and 5 (yellow circles). In detail, on 26 June negative absolute vorticity is visible at no. 2, 3, 5, and 7. But within the subsequent 3 days, anticyclonic eddies have only developed at sites no. 2 and 5. It is common to these sites that the coast is on the right, relative to the current direction, and that the relative vorticity is anticyclonic due to the no-slip condition at the lateral solid boundaries. However, at sites no. 2 and 5, the curvature of the coastline is anticyclonic in contrast to the other sites. Apparently, a solid boundary on the right and anticyclonic curvature of that boundary, are additional necessary conditions for the formation of eddies driven by inertial instability. These conditions are also satisfied at site no. 7, but there is no indication for eddy growth. It is most likely prevented by the southward current with cyclonic vorticity along the west coast of the island. The above findings are in agreement with Väli et al. (2017) who found values of $\zeta/f < -1$ at various near-coast locations in the Gulf of Finland. Gula et al. (2016b) showed that equivalent conditions were satisfied in the Gulf Stream where the anticyclonic shear is amplified by the topographic drag against the slopes of the Great and Little Bahama Banks on its way through the Florida Straits. A similar situation is given where the California Undercurrent passes along Point Sur Ridge, a topographic obstacle near Monterey Bay (Dewar et al., 2015; Molemaker et al., 2015). Both cases lead to the formation of unstable submesoscale fronts and eddies.

According to Thomas et al. (2013), symmetric instability occurs when

$$\phi_{Ri_{geo}} < \phi_c \quad , \quad (10)$$

with

$$\phi_{Ri_{geo}} = \tan^{-1} \left(-\frac{1}{Ri_{geo}} \right) \quad (11)$$

and

$$\phi_c = \tan^{-1} \left(-\frac{\zeta_{geo}^a}{f} \right) \quad . \quad (12)$$

Here,

$$Ri_{geo} = \frac{f^2 N^2}{|\nabla_h b|^2} \quad (13)$$

is the Richardson number of the geostrophic flow,

$$b = -\frac{g\rho}{\rho_0} \quad (14)$$

is the buoyancy,

$$N^2 = -\frac{g}{\rho_0} \frac{\partial \rho}{\partial z} \quad (15)$$

the squared Brunt-Väisälä frequency, and

$$\zeta_{geo}^a = f + \frac{\partial v_{geo}}{\partial x} - \frac{\partial u_{geo}}{\partial y} \quad (16)$$

the absolute vorticity of the geostrophic flow $\mathbf{V}_{geo} = (u_{geo}, v_{geo})$. ρ_0 is a constant reference density, and g the gravitational acceleration. Specifically, in regions where $\zeta_{geo}^a/f > 1$ (cyclonic vorticity), symmetric instability prevails, if the conditions

$$C_{SI} = -90^\circ < \phi_{Ri_{geo}} < \phi_c \quad \wedge \quad \phi_c < -45^\circ \quad (17)$$

are satisfied. By contrast, symmetric instability is the dominant mode of instability in regions of anticyclonic vorticity ($\zeta_{geo}^a/f < 1$), if

$$C_{SI} = -90^\circ < \phi_{Ri_{geo}} < -45^\circ \quad \wedge \quad \phi_c > -45^\circ \quad . \quad (18)$$

As the condition described by eq. (10) must be satisfied in the mixed layer for symmetric instability to occur, all above quantities were evaluated in R100 at 2-m depth. Note that the relative vorticity is identical to the relative vorticity of the geostrophic flow, because ζ is the curl of the rotational, divergence-free part of the total velocity which is the geostrophic velocity by definition. Hence, a decomposition of the total velocity in a geostrophic part \mathbf{V}_{geo} and an ageostrophic part \mathbf{V}_{ageo} requiring a Poisson solver is redundant (for some test cases, both ζ_{geo} and ζ were evaluated showing identical results). For simplification, the subscript “geo” will therefore be dropped for ζ_{geo}^a and Ri_{geo} . Fig. 14 shows ϕ_{Ri} , ϕ_c , and C_{SI} at the start of the model integration on 15 June (using as initial condition when the corresponding field is mapped from R500 on the 100-m grid), and on 26 June. On 15 June, there are large areas where $-90^\circ < \phi_{Ri} < -45^\circ$ (Fig. 14a, in blue), indicating satisfaction of the first condition of eqs. (17) and (18). However, this condition is only necessary and sufficient for regions of cyclonic vorticity ($\phi_c < -45^\circ$). Considering the second condition in eq. (18), necessary and sufficient conditions for regions of anticyclonic vorticity are satisfied, if, and only if, $\phi_c > -45^\circ$. Linking the requirements for ϕ_c (Fig. 14c) and ϕ_{Ri} yields the logical map Fig. 14e for 15 June, indicating where eqs. (17) and (18) are satisfied for cyclonic and anticyclonic vorticity, respectively. Compared to the fairly widespread areas where the necessary conditions for ϕ_{Ri} and ϕ_c are met separately, the necessary and sufficient conditions for C_{SI} are satisfied only in rather limited streaks. Nine days later, on 26 June, there are just a few spots where even C_{SI} is satisfied (Fig. 14f). Hence, favourable conditions for symmetric instability prevail only during the initial phase of the model integration, becoming less frequent thereafter. More insight into the temporal evolution of the statistics of C_{SI} is provided by the relative frequency of occurrence, $p(C_{SI}) = 100 \cdot n(C_{SI} \equiv true)/N$, where n is the number of grid cells where the criterion for C_{SI} is met, and N is the total number of grid cells. $p(C_{SI})$ decays from 4.8 % on 15 June to 1.8 % on 16 June, which yields an e-folding scale of ≈ 1 day comparable to the inertial period of 14.6 h at this latitude. Thereafter, $p(C_{SI})$ decreases almost steadily and stabilises around 0.5 %. Hence, as symmetric instability extracts kinetic energy from the geostrophic flow at a rate given by the geostrophic shear production (Thomas et al., 2013), this process comes rapidly due to a halt after about one inertial period and mixed-layer instability, presumably, takes over. $p(C_{SI})$ was also computed for the R100 model run with atmospheric forcing (see above Section 4.3). In that run, $p(C_{SI})$ increased strongly on 18, 21, 24, and 27 June, which were the times of the wind bursts (cf. Fig. 3), and slackened thereafter. Thus, the conditions

favouring symmetric instability are re-established during strong wind events by the buildup of kinetic energy, and as soon as the wind slackens, the energy is released.

Mixed-layer instability is an efficient mechanism to restratify the mixed layer (Boccaletti et al., 2007). For the determination of the mixed-layer depth, MLD, a $\Delta\sigma_\theta = 0.1 \text{ kg m}^{-3}$ criterion was used, i.e. MLD was defined as the depth where the potential density exceeds the surface density for the first time by $\Delta\sigma_\theta$. The domain-wide mean MLD decreases almost linearly from 12.7 m on 15 June to 5.1 m on 29 June. Hence, the mixed-layer is restratified, probably by mixed-layer instability. In order to exclude that symmetric instability drives the restratification, the relative frequency of occurrence, $p(Ri) = 100 \cdot n(Ri < 1)/N$, was computed. This quantity drops from 23.2 to 4.0 % within the first day of the integration and decreases thereafter slowly to 1.4 % on 29 June. Hence, after about one inertial period, $Ri \geq 1$ almost everywhere, which makes symmetric instability unlikely. This is in accordance with Haine and Marshall (1998) who state that “symmetric instability rapidly generates a layer with vanishing potential vorticity ($Ri = 1$), but non-zero vertical stratification. Thereafter a nonhydrostatic baroclinic instability develops ...”.

4.4.4 Frontal circulation

In order to provide details of the secondary circulation in submesoscale fronts in a non-idealised model, features resembling the confluence situation as provided by a deformation field were identified in the R100 fields of 26 June in the red box indicated in Fig. 7d. Here, dense water in the east and light water in the west, form a confluent flow pattern and generate a density contrast at the surface of more than 0.4 kg m^{-3} over a horizontal distance of about 2 km within the black rectangle shown in Fig. 15.

Detailed maps of various quantities within that rectangle are displayed in Fig. 16a–e, and vertical cross sections along the dashed lines are shown in Fig. 16f–j. In the western part of the front, the total velocity vectors at the surface are aligned almost parallel to the isopycnals (panel a); extreme values of $|\mathbf{V}|$ are close to 12 cm s^{-1} at the surface. In the cross section (panel f), the v component attains minimum values of $< -10 \text{ cm s}^{-1}$, located by a few hundred metres to the west of the maximum horizontal density gradient (panel b). The velocity field depicts the classical picture of a frontal jet, with a width of about 3 km and the depth around 4 m. It is defined by the -6 cm s^{-1} isotach of the v -component. The horizontal shear of the jet creates a front-parallel band of strong cyclonic relative vorticity with maximum values of $> 1.6f$ (panels c, h). The cross-front width of the band is about 600 m, and the highest values of the relative vorticity are congruent with the maximum horizontal density gradient (panel b). A wide band of anticyclonic relative vorticity extends to the west of the cyclonic region. East of the cyclonic region, several bands with alternating sign are aligned. Vectors of \mathbf{V}_{geo} are superimposed in panel c. A comparison with panels a and c reveals, that the directions of \mathbf{V} and \mathbf{V}_{geo} resemble closely each other in appearance, but the speeds are slightly different. While the maximum speeds of \mathbf{V} are around 12 cm s^{-1} in the jet, those of \mathbf{V}_{geo} are close to 10 cm s^{-1} i.e. the jet is super-geostrophic (Persson, 2001). This is confirmed by panel d which shows the horizontal divergence δ/f , together with the vectors of the ageostrophic flow \mathbf{V}_{ageo} : the meridional components of \mathbf{V}_{ageo} and \mathbf{V}_{geo} have the same (negative) sign, hence \mathbf{V}_{ageo} amplifies the geostrophic jet. The maximum ageostrophic speeds are around 6 cm s^{-1} . In the cross-frontal direction (panel g), the 5.25 kg m^{-3} isopycnal separates two regimes of opposite zonal component of the ageostrophic flow,

u_{ageo} : in the lighter water, $u_{ageo} > 0$, and $u_{ageo} < 0$ in the heavier water. While the overall magnitude of u_{ageo} is just a few mm s^{-1} , it attains its highest value of about 1 cm s^{-1} right at the location of the surface outcrop of the 5.25 kg m^{-3} isopycnal.

The impact of \mathbf{V}_{ageo} on the divergence δ and on the vertical speed w is illustrated in Figs. 16d, i, e, and j. According to panels d and i, extreme values of $\delta/f \approx 0.3$ and $\delta/f \approx -0.8$ are found at the sea surface immediately to the west and to the east of the maximum horizontal density gradient, respectively. The minimum of the divergence (=maximal convergence) drives a deep-reaching downwelling cell with extreme speeds of almost 15 m day^{-1} . Less intense upwelling of maximal $\approx 6 \text{ m day}^{-1}$ is associated with the divergence maximum (panel j). The positions of the extrema of δ/f are also reflected by its horizontal surface distribution in panel d, while a comparison of panels d and e reveals a clear correlation between δ and w . Patches of convergent motion are found also along the 5.25 kg m^{-3} isopycnal in panel i; potentially, they feed the large downwelling area underneath it. Further cells of intense vertical motion are found west and east of the surface front as shown in panel j. Apparently, these patterns are not parts of the secondary circulation, but rather caused by internal waves (see Section 4.2.3) or by another weak front located about 600 m further east.

Overall, the described secondary circulation pattern closely resembles the ones of the idealised model studies mentioned in the Introduction; primarily, this is a “single overturning cell with upwelling and surface divergence on the light side and downwelling and surface convergence on the dense side” (literally after McWilliams (2016)). However, Fig. 16 provides additional details which were potentially not yet highlighted before:

- The frontal jet is super-geostrophic, i.e. the jet speed is amplified by an ageostrophic component. Under the assumption that the jet was in geostrophic balance, the theoretical inclination of the front was calculated as 0.003° using the Margules equation (Margules, 1906). Assuming the $\sigma_\theta = 5.25 \text{ kg m}^{-3}$ isopycnal as the frontal interface, the tilt angle of that isopycnal was, however, only 0.001° . Hence, the slope of the front is not in geostrophic balance with the jet. This circumstance was not considered in the previous literature, assuming two-dimensionality (Bleck et al., 1988), or quasi-geostrophic (Nagai et al., 2006), or semi-geostrophic (Thompson, 2000) balance. In contrast, in the model of McWilliams (2017) (see Fig. 5 there), the ageostrophic contribution to the jet speed amounts to about 3 cm s^{-1} while the geostrophic fraction is close to 12 cm s^{-1} .
- The maximum speed of the cross-frontal ageostrophic velocity is weaker than expected from earlier models. Right at the surface, it is only 1 cm s^{-1} , while Bleck et al. (1988) arrived at $> 4.5 \text{ cm s}^{-1}$ and McWilliams (2017) at least at 2 cm s^{-1} . A potential reason for this discrepancy is that the other studies did not consider the ageostrophic velocity as being the ageostrophic part of the total flow, but rather as the departure from the (barotropic) deformation velocity or from the far-field average, instead. In the present situation, it was not possible to separate the total flow into such components because they were not defined. Hence, one may speculate that something like the deformation velocity is opposed to the cross-front ageostrophic velocity and attenuates it.
- According to Fig. 16g, the cross-frontal velocity is positive (eastward) in the light water ($\sigma_\theta < 5.25 \text{ kg m}^{-3}$) and westward in the denser water below. Thus, the velocity converges at that isopycnal, in accordance with Fig. 16i. It is not known to the authors whether such a “sloping convergence” was mentioned before in the oceanographic literature.

The investigated front satisfies the criteria to be denoted as “submesoscale”. The first criterion, $Ro \sim \mathcal{O}(1)$, is confirmed by Figs. 16c and h, indicating that the f -scaled relative vorticity (which is equivalent to a local Rossby number) is $\mathcal{O}(1)$. Another criterion is $Ri \sim \mathcal{O}(1)$ (Thomas et al., 2008; Mahadevan, 2016). According to Fig. 17, $Ri \approx 2$ in the frontal region at the location of maximum convergence at the sea surface.

5 5 Comparison of features with observations

The R100 results presented above have provided a detailed insight into STPPs, such as tracer patterns, kinematic structures, and dynamical processes related to fronts and eddies. A comparison with observations, however, is rather limited because STPPs are difficult to measure due to their small spatial and temporal scales. Moreover, the R100 results are obtained from a run without atmospheric forcing, and it would be legitimate to compare them only with situations where the air-sea fluxes of momentum, heat, and freshwater are minimum. However, the atmospheric conditions not to mention the air-sea fluxes when the observations were taken, are mostly not described. Hence, the comparisons below based on a few statistical numbers and qualitative similarities should be handled with care.

Kinematic quantities of STPPs were obtained from direct measurements in the framework of the LatMix and SubEx experiments. Shcherbina et al. (2013) presented a detailed view of submesoscale vorticity, divergence, and strain statistics from synchronous two-ship ADCP (Acoustic Doppler Current Profiler) samplings. Specifically, their observations indicated flows with $Ro \sim \mathcal{O}(1)$ and an asymmetry in the distribution of the relative vorticity skewed towards positive values. The latter is in excellent agreement with the R100 results. By contrast, Ohlmann et al. (2017) identified STTPs with aerial guidance and seeded them with drifters. The Lagrangian observations exhibited high values of relative vorticity and divergence exceeding $5f$, suggesting vertical velocities up to 240 m day^{-1} . Such values are rather close to the peak values obtained from R100. Similar values for ζ/f and δ/f resulted also from the high-frequency radar observations of Parks et al. (2009). As the observations mentioned above are two-dimensional and confined to the sea surface, they provide only limited information of subsurface properties of STPPs. Somewhat more detailed insight is gained from the high-resolution in-situ measurements of Zhong et al. (2017) which exhibit submesoscale kinematic structures along a vertical section through a 200 km wide mesoscale eddy in the South China Sea. Unfortunately, that eddy is an anticyclone and a comparison with the corresponding quantities in C3 is problematic.

The formation of a the submesoscale cyclonic eddy C3 (Fig. 12) resembles closely the sequence of infrared images published by Munk et al. (2000) (see Fig. 12 there) and the snapshot of Buckingham et al. (2017). In both cases, the eddies originate from an unstable thermal front which finally breaks up in a train of cyclonic eddies. While the diameters of the eddies shown by Munk et al. (2000) are around 10 km (very rough visual estimate), those of Buckingham et al. (2017) are smaller (1–10 km according to the authors).

A closeup infrared image of an eddy observed in the Southern California Bight is shown in Fig. 18, together with corresponding properties from the modelled cyclone C3 (see Figs. 11, 12). The observed sea surface temperature (panel a) exhibits a spiraliform cyclonic eddy with a diameter of about 1 km, where the diameter is estimated as the width between the $\approx 13.8^\circ\text{C}$

isotherms (purple) on either side. Special features are the low temperature patches (black) close to the eddy centre suggesting upwelling, and the bright ripples in the southwest which are probably caused by internal waves. One may note also the cold spots “S” along the periphery; they are definitely not caused by a malfunction of the camera, because they show up at different positions in a sequence of images taken within a period of about 20 minutes. Potentially, they are created by intense vertical mixing (cf. Figure 2 in Marmorino et al. (2018)). For comparison with C3, the potential temperature and salinity at 15 m depth are provided in panels b and c. This depth was selected as the mixed-layer depth at the corresponding position in R100 is about 9 m and the surface signal of C3 is hardly resolved (cf. potential temperature and salinity on 26 June in Fig. 5). The overall structures of the C3 salinity and the sea surface temperature of the observed eddy are looking similar but the smaller details visible in the latter are not reproduced by C3: these are the ripples in the southwest, the cold spots, and as well the texture of the tracer field in the core. Most probably, this is due to the insufficient horizontal resolution of R100 or non-hydrostatic effects which are not included in the applied ROMS version.

There are two observational studies available regarding necessary instability criteria at fronts (Thomas et al., 2013; Zhong et al., 2017) but they are not comparable to the maps in Fig. 14 because the criteria were computed along vertical sections across the Gulf Stream front and in a large anticyclonic eddy in the South China Sea, respectively. Concerning frontogenetic or frontolytic processes, computations or estimations of the components of the frontal tendency equation from observational data are not known to the authors.

Comprehensive observations of the frontal circulation (Pollard and Regier, 1992; Rudnick, 1996; Pallàs-Sanz et al., 2010) confirm the secondary circulation pattern as predicted from theoretical considerations and numerical models. However, the above studies did not resolve STTPs and the extrema of the vertical velocity are correspondingly low with $\mathcal{O}(10 \text{ m day}^{-1})$. Namely, the vertical velocities in the front shown in Fig. 16e and j are on the same order but this is due to the low water depth. On the contrary, the higher-resolution observations of a submesoscale front oriented along the periphery of a mesoscale eddy (Adams et al., 2017) confirm vertical velocities of $\mathcal{O}(100 \text{ m day}^{-1})$. Moreover, it was demonstrated that within the same front existed confluent and diffluent regions of the cross-frontal velocity. This does not necessarily prove that the ageostrophic velocity changes sign, but it indicates that the generally accepted picture of the secondary circulation is only valid in the case of frontogenesis driven by an externally imposed deformation field.

6 Conclusions

A double one-way nesting approach is used in order to simulate submesoscale turbulent patterns and processes (STPPs) in the southern Baltic Sea in summer 2016. In order to reproduce the mesoscale environment in a realistic way, the Regional Ocean Modeling System (ROMS) with 500-m horizontal resolution (R500) is nested in an existing operational model, and further downscaling to a grid size of 100 m (R100) enables the generation of STPPs.

In R500, the kinematic and dynamical structures are rather sensitive to the surface boundary conditions. While the response of mesoscale patterns to the turning-off of the atmospheric forcing is rather sluggish, it has an immediate impact on the

generation of smaller-scale features which represent already the low-wavenumber part of submesoscale turbulence in the spectral range around 5 km.

In R100, the atmospheric forcing is turned-off from the outset because the air-sea fluxes inhibit the growth of STTPs. Thus, the R100 results represent situations that occur only under quasi-adiabatic conditions. In Nature, such situations are approximated in no-wind or light-wind conditions which offer the best chance to observe STTPs. On the other hand, the R100 findings must not be compared to observations which are taken during stronger wind. Moreover, as the R100 findings reflect summer conditions in the Baltic Sea, they must not be applied to another season or any other region of the World Ocean.

The horizontal density gradients in R100 grow for about 10 days, and afterwards the frequency of occurrence of strong gradients begins to decline, indicating frontal arrest as soon as the absolute horizontal density gradient reaches a critical value. STTPs develop rapidly within about a day; they are characterised by relative vorticities and divergences reaching multiple of the Coriolis parameter, where the frequency distribution of relative vorticity is clearly biased towards negative (anticyclonic) values. Vertical velocities of $\mathcal{O}(100)$ m day⁻¹ are diagnosed in R100. However, as the vertical motion is predominantly controlled by internal waves and to a lesser extent by frontal secondary circulations, estimates of the vertical velocities associated with submesoscale processes are one order of magnitude less.

Typical elements of the secondary circulation of two-dimensional strain-induced frontogenesis are identified at an exemplary front in shallow water; these are the frontal jet, the downwelling on the dense side and upwelling on the less dense side. In addition to the results of idealised two-dimensional models, details of the ageostrophic current field and the related divergence are revealed: the frontal jet is not in geostrophic balance but super-geostrophic, instead. Further on, it is shown that a region of enhanced convergent flow is aligned with the slope of the frontal surface.

The components of the tendency equation are evaluated in a subregion of the R100 domain. At fronts, frontogenetic and frontolytic processes represented by the frontogenetic tendency, F , and the contributions from the straining deformation of the geostrophic and vertical velocity, Q_{geo} and Q_w , respectively, are equipartioned, bimodal, and of the same order of magnitude. By contrast, the contributions from the ageostrophic velocity, Q_{ageo} , and from vertical mixing, Q_{dv} , act primarily frontogenetic while the contribution from horizontal mixing, Q_{dh} , is negligible everywhere.

The conditions for two types of hydrodynamic instability are evaluated for the whole R100 domain: favourable conditions for inertial (centrifugal) instability are found only along coastlines. There, anticyclonic eddies develop rapidly from along-coast currents if the coast is on the right hand side (looking downstream) and if the coastline is anticyclonically curved. During the first day of the R100 integration, symmetric instability is likely to occur in about 5 % of the model domain but within two days, the probability drops to <1 %. Parallel to the rapidly decreasing probability increases the geostrophic Richardson number Ri_{geo} . While at the beginning of the integration, $Ri_{geo} < 1$ in about 24 % of the R100 domain, this number decreases to about 4 % after one day, indicating that mixed-layer instability is the main process depleting the reservoir of potential energy.

While anticyclonic eddies are generated solely along coastlines due to inertial instability, cyclonic eddies are found in the entire R100 domain, but preferably in those regions where the water depth is less than about 40 m. A special feature of the cyclones is their ability to absorb internal waves and to sustain patches of continuous upwelling for several days favouring plankton growth (Mahadevan, 2016). By contrast to mesoscale cyclones which pinch off from basin-scale fronts, submesoscale

cyclones are rolled-up streamers, similar to those observed by Klymak et al. (2016) on the north wall of the Gulf Stream. Hence, it may not be appropriate to denote these features “eddies” but “spirals” instead, as suggested by Munk et al. (2000).

A peculiar feature of the observed eddy shown in 18a are the cold spots along its periphery. It is conjectured that the spots are small upwelling cells probably driven by gravitational instability which links the submesoscale with the microscale and finally leads to three-dimensional energy dissipation. As it is extremely challenging to observe such features with in situ methods, attempts will be made to catch these spots with further downscaling to the $\mathcal{O}(1)$ m scale using non-hydrostatic models or Large Eddy Simulations. These numerical approaches would also serve to explore structures and processes in the interior of eddies in greater detail.

Code and data availability. The model code and the output of the ROMS runs presented in this article are available from the first author on request.

Author contributions. Reiner Onken implemented the double-nested ROMS model for the given region in the Baltic Sea and conducted the model runs. Ingrid M. Angel-Benavides and Burkard Baschek contributed the results from the SubEx experiment in the Southern California Counter Current, and Burkard Baschek coordinated the “Expedition Clockwork Ocean” and the corresponding modeling activities.

Competing interests. The authors declare that they have no conflicts of interest.

Acknowledgements. We thank Rüdiger Röttgers and Hajo Krasemann for the processing of Fig. 4b, and Rainer Feistel who provided details of the Arkona and Bornholm Basins to us. Geoffrey Smith and George Marmorino, Naval Research Laboratory, provided infrared observations taken during the Submesoscale Experiments for comparison. The ICON-EU output was made available by Thomas Bruns of the German Weather Service (DWD). The output of the HIROMB-BOOS model was downloaded from the Copernicus Marine Environment Monitoring Service, and the bathymetry data from the General Bathymetric Chart of the Oceans were provided by the British Oceanographic Data Centre. The coastline data were obtained from NOAA (National Oceanic and Atmospheric Administration).

References

- Adams, K. A., Hosegood, P., Taylor, J. R., Sallée, J. B., Bachman, S., Torres, R., and Stamper, M.: Frontal circulation and submesoscale variability during the formation of a Southern Ocean mesoscale eddy. *Journal of Physical Oceanography*, 47, 1737–1753, doi: 10.1175/JPO-D-16-0266.1, 2017.
- 5 Berg, P. Mixing in HBM. DMI Scientific Report, 12-03, Danmarks Meteorologiske Institut, København, Denmark, 2012.
- Bleck, R., Onken, R., and Woods, J. D.: A two-dimensional model of mesoscale frontogenesis in the ocean. *Quartely Journal of the Royal Meteorological Society*, 114, 347–371, 1988.
- Blumen, N.: On short-wave baroclinic instability. *Journal of Atmospheric Sciences*, 36, 1925–1933, 1979.
- Boccaletti, G., Ferrari, R., and Fox-Kemper, B.: Mixed layer instabilities and restratification. *Journal of Physical Oceanography*, 37, 2228–2250, doi: 10.1175/JPO3101.1, 2007.
- 10 Buckingham, C. E., Khaleel, Z., Lazar, A., Martin, A. P., Allen, J. T., Naveira Garabato, A. C., Thompson, A. F., and Vic, C.: Testing Munk’s hypothesis for submesoscale eddy generation using observations in the North Atlantic. *Journal of Geophysical Research Oceans*, 122, 6725–6745, doi: 10.1002/2017JC012910, 2017.
- Charney, J. G.: Geostrophic turbulence. *Journal of Atmospheric Sciences*, 28, 1087–1095, 1971.
- 15 Capet, X., McWilliams, J. C., Molemaker, M. J., and Shchepetkin, A. F.: Mesoscale to submesoscale transition in the California Current system. Part I: flow structure, eddy flux, and observational tests. *Journal of Physical Oceanography*, 38, 29–43, doi: 10.1175/2007JPO3671.1, 2008a.
- Capet, X., McWilliams, J. C., Molemaker, M. J., and Shchepetkin, A. F.: Mesoscale to submesoscale transition in the California Current system. Part II: frontal processes. *Journal of Physical Oceanography*, 38, 44–64, doi: 10.1175/2007JPO3672.1, 2008b.
- 20 Capet, X., McWilliams, J. C., Molemaker, M. J., and Shchepetkin, A. F.: Mesoscale to submesoscale transition in the California Current system. Part III: energy balance and flux. *Journal of Physical Oceanography*, 38, 2256–2269, doi: 10.1175/2008JPO3810.1, 2008c.
- Chapman, D. C.: Numerical treatment of cross-shelf open boundaries in a barotropic coastal ocean model. *Journal of Physical Oceanography*, 15, 1060–1075, 1985.
- Charney, J. P.: The dynamics of long waves in a baroclinic westerly current. *Journal of Meteorology*, 4, 135–163, 1947.
- 25 Dewar, W. K., McWilliams, J. C., and Molemaker, M. J.: Centrifugal instability and mixing in the California Undercurrent. *Journal of Physical Oceanography*, 45, 1224–1241, doi: 10.1175/JPO-D-13-0269.1, 2015.
- Eady, T.: Long waves and cyclone waves. *Tellus*, 1, 33–52, 1949.
- Eliassen, A.: On the vertical circulation in frontal zones. *Geofysiske Publikasjoner* 24, 147–160, 1962.
- Fairall, C. W., Bradley, E. F., Rogers, D. B., Edson, J. B., and Young, G. S.: Bulk parameterization of air-sea fluxes for Tropical Ocean-Global Atmosphere Coupled-Ocean Atmosphere Response Experiment. *Journal of Geophysical Research*, 101, C2, 3747–3764, doi: 10.1029/95JC03205, 1996.
- 30 Feistel, R., Nausch, G., and Wasmund, N. (Eds.): State and Evolution of the Baltic Sea, 1952–2005: A Detailed 50-year Survey of Meteorology and Climate, Physics, Chemistry, Biology, and Marine Environment. Wiley-Interscience, Hoboken, New Jersey, USA, ISBN 978-0-471-97968-5, 2008.
- Fennel, W., Seifert, T., and Kayser, B.: Rossby radii and phase speeds in the Baltic Sea. *Continental Shelf Research*, 11 (1), 23–26, 1991.
- Fox-Kemper, B., and Ferrari, F.: Parameterization of mixed layer eddies. Part I: theory and diagnosis. *Journal of Physical Oceanography*, 38, 1145–1165, doi: 10.1175/2007JPO3792.1, 2008.

- Früh, W.-G.: Amplitude vacillation in baroclinic flows. In: von Larcher, T., and Williams, P. D. (Eds.): *Modelling Atmospheric and Oceanic Flow: Insights from laboratory experiments and numerical simulations*. Wiley, pp. 61–81, doi: 10.1002/9781118856024, 2015.
- Gula, J., Molemaker, M. J., and McWilliams, J. C.: Submesoscale cold filaments in the Gulf Stream. *Journal of Physical Oceanography*, 44, 2617–2643, doi: 10.1175/JPO-D-14-0029.1, 2014.
- 5 Gula, J., Molemaker, M. J., and McWilliams, J. C.: Submesoscale dynamics of a Gulf Stream frontal eddy in the South Atlantic Bight. *Journal of Physical Oceanography*, 46, 305–325, doi: 10.1175/JPO-D-14-0258.1, 2016a.
- Gula, J., Molemaker, M. J., and McWilliams, J. C.: Topographic generation of submesoscale centrifugal instability and energy dissipation. *Nature Communications*, 7:12811, doi: 10.1038/ncomms12811, 2016b.
- [Gurova, E., and Chubarenko, B. : Remote-sensing observations of coastal sub-mesoscale eddies in the south-eastern Baltic. *Oceanologia*, 54\(4\), 631–654, doi: 10.5697/oc.54-4.631, 2012.](#)
- 10 [Haine, T. W. N., and Marshall, J.: Gravitational, symmetric, and baroclinic instability of the ocean mixed layer. *Journal of Physical Oceanography*, 28, 634–658, 1998.](#)
- Haney, R. L.: On the pressure gradient force over steep topography in sigma coordinate models. *Journal of Physical Oceanography*, 21, 610–619, 1991.
- 15 Haidvogel, D. B., Arango, H. G., Hedström, K., Beckmann, A., Malanotte-Rizzoli, P., and Shchepetkin, A. F.: Model evaluation experiments in the North Atlantic Basin: simulations in nonlinear terrain-following coordinates. *Dynamics of Atmospheres and Oceans*, 32, 239–281, 2000.
- Hide, R.: An experimental study of thermal convection in a rotating liquid. *Philosophical Transactions of the Royal Society of London (A)*, 250, 441–478, 1958.
- 20 Holton, J.: The role of gravity induced drag and diffusion in the momentum budget of the mesosphere. *Journal of the Atmospheric Sciences*, 39, 791–79, 1982.
- Holton, J. R.: *An introduction to dynamic meteorology*. Fourth edition, Elsevier Academic Press, ISBN: 0-12-354016-X, 2004.
- Hoskins, B. J.: The mathematical theory of frontogenesis. *Annual Reviews of Fluid Mechanics*, 14, 131–151, 1982.
- Kantha, L. H., and Clayson, C. A.: An improved mixed-layer model for geophysical applications. *Journal of Geophysical Research*, 99, 25235–25266, 1994. [Karimova2016](#)
- 25 [Karimova, S., and Gade, M.: Improved statistics of submesoscale eddies in the Baltic Sea retrieved from SAR imagery. *International Journal of Remote Sensing*, 37\(19\), 2394–2414, doi: 10.1080/01431161.2016.1145367, 2016.](#)
- Klymak, J. M., Shearman, R. K., Gula, J., Lee, C. M., D’Asaro, E. A., Thomas, L. N., Harcourt, R. R., Shcherbina, A. Y., Sundermeyer, M. A., Molemaker, J., and McWilliams, J. C.: Submesoscale streamers exchange water on the north wall of the Gulf Stream. *Geophysical Research Letters*, 43, 1226–1233, doi: 10.1002/2015GL067152, 2016.
- 30 Kubryakov A. A., and Stanichny, S. V.: Seasonal and interannual variability of the Black Sea eddies and its dependence on characteristics of the large-scale circulation, *Deep-Sea Research I*, 97, 80–91, doi: <https://doi.org/10.1016/j.dsr.2014.12.002>, 2015.
- Large, W. G., McWilliams, J. C., and Doney, S. C.: Oceanic vertical mixing: a review and a model with a nonlocal boundary layer parameterization. *Reviews in Geophysics*, 32, 363–403, 1994.
- 35 Lévy, M., Ferrari, R., Franks, P. J. S., Martin, A. P., Rivière, P.: Bringing physics to life at the mesoscale. *Geophysical Research Letters*, 39, L14602, doi: 10.1029/2012GL052756, 2012.
- Leppäranta, M., and Myrberg, K. (Eds.): *Physical Oceanography of the Baltic Sea*. Springer, Berlin, ISBN 978-3-540-79702-9, 2009.
- Magaard, L., and Rheinheimer, G. (Eds.): *Meereskunde der Ostsee*. Springer-Verlag, Berlin, 269 pp, 1974.

- Mahadevan, A.: The impact of submesoscale physics on primary productivity of plankton. *Annual Review of Marine Science*, 8, 161–184, doi: 10.1146/annurev-marine-010814-015912, 2016.
- Mahadevan, A., Tandon, A., and Ferrari, R.: Rapid changes in mixed layer stratification driven by submesoscale instabilities and winds. *Journal of Geophysical Research*, 115, C03017, doi: 10.1029/2008JC005203, 2010.
- 5 Marmorino, G. O., Smith, G. B., and Miller, W. D.: Surface imprints of water-column turbulence: a case study of tidal flow over an estuarine sill. *Remote Sensing*, 5, 3239–3258, doi: 10.3390/rs5073239, 2013.
- Marmorino, G. O., Smith, G. B., North, R. P., and Baschek, B.: Application of airborne infrared remote sensing to the study of ocean submesoscale eddies. *Frontiers in Mechanical Engineering*, 4(10), doi: 10.3389/fmech.2018.00010, 2018.
- 10 Marchesiello, P., McWilliams, J. C., and Shchepetkin, A. F.: Open boundary conditions for long-term integration of regional ocean models. *Ocean Modelling*, 3, 1–20, 2001.
- Margules, M.: Über Temperaturschichtung in stationär bewegter und in ruhender Luft. *Meteorologische Zeitschrift*, Hann-Volume, 243–254, 1906. Translated and edited by Volken, E., Giesche, A., and Brönnimann, S.: On temperature stratification in resting and non-accelerated moving air. *Meteorologische Zeitschrift*, 25, 6, 795–804, doi: 10.1127/metz/2016/0833, 2016.
- 15 McWilliams, J. C.: Fluid dynamics at the margin of rotational control. *Environmental Fluid Mechanics*, 8, 441–449, doi: 10.1007/s10652-008-9081-8, 2008.
- McWilliams, J. C.: Submesoscale currents in the ocean. *Proceedings of the Royal Society A* 472: 20160117, doi: 10.1098/rspa.2016.0117, 2016.
- McWilliams, J. C.: Submesoscale surface fronts and filaments: secondary circulation, buoyancy flux, and frontogenesis. *Journal of Fluid Mechanics*, 823, 391–432, doi: 10.1017/jfm.2017.294, 2017.
- 20 [McWilliams, J. C.: A survey of submesoscale currents. *Geoscience Letters*, 6:3, doi: 10.1186/s40562-019-0133-3, 2019.](#)
- McWilliams, J. C., Molemaker, M. J., and Olafsdottir, E. I.: Linear fluctuation growth during frontogenesis. *Journal of Physical Oceanography*, 39, 3111–3129, doi: 10.1175/2009JPO4186.1, 2009.
- Molemaker, M. J., McWilliams, J. C., and Dewar, W. K.: Submesoscale instability and generation of mesoscale anticyclones near a separation of the California Undercurrent. *Journal of Physical Oceanography*, 45, 613–629, doi: 10.1175/JPO-D-13-0225.1, 2015.
- 25 Müller, P., McWilliams, J. C., and Molemaker, J.: The 2D/3D turbulence conundrum. In: Baumert, H. Z., Simpson, J., and Sündermann, J. (eds.) *Marine Turbulence: theories, observations and models*. Cambridge University Press, Cambridge, 397–505, 2008.
- Munk, W., Armi, L., Fischer, K., and Zachariasen, F: Spirals on the sea. *Proceedings of the Royal Society A*, 456, 1217–1280, 2000.
- Nagai, T., Tandon, A., and Rudnick, D. L.: Two-dimensional ageostrophic secondary circulation at ocean fronts due to vertical mixing and large-scale deformation. *Journal of Geophysical Research*, 111, C09038, doi: 10.1029/2005JC002964, 2006.
- 30 Ohlmann, J. C., Molemaker, M. J., Baschek, B., Holt, B., Marmorino, G., and Smith, G.: Drifter observations of submesoscale flow kinematics in the coastal ocean. *Geophysical Research Letters*, 44, 330–337, doi: 10.1002/2016GL071537, 2017.
- Onken, R.: Mesoscale upwelling and density finestructure in the seasonal thermocline – a dynamical model. *Journal of Physical Oceanography*, 22, 11, 1257–1273, 1992.
- 35 Onken, R.: Validation of an ocean shelf model for the prediction of mixed-layer properties in the Mediterranean Sea west of Sardinia. *Ocean Science*, 13, 235–257, doi: 10.5194/os-13-235-2017, 2017.
- Osinski, R., Rak, D., Walczowski, W., and Piechura, W.: Baroclinic Rossby radius of deformation in the southern Baltic Sea. *Oceanologia*, 52(3), 417–429, 2010.

- Pallàs-Sanz, E., Johnston, T. M. S., and Rudnick, D. L.: Frontal dynamics in a California Current System shallow front: 1. Frontal processes and tracer structure. *Journal of Geophysical Research*, 115, C12067, doi: 10.1029/2009JC006032, 2010.
- Parks, A. B., Shay, L. K., Johns, W. E., Martinez-Pedraja, J., and Gurgel, K.-W.: HF radar observations of small-scale surface current variability in the Straits of Florida. *Journal of Geophysical Research*, 114, C08002, doi: 10.1029/2008JC005025, 2009.
- Persson, A.: The Coriolis force and the geostrophic wind (Coriolis Part 5). *Weather*, 56, 267–272, doi: 10.1002/j.1477-8696.2001.tb06589.x, 2001.
- Plougonven, R., and Snyder, C.: Inertia-gravity waves spontaneously generated by jets and fronts. Part I: Different baroclinic life cycles. *Journal of the Atmospheric Sciences*, 64, 2502–2520, doi: 10.1175/JAS3953.1, 2007.
- Pollard, R. T., and Regier, L. A.: Vorticity and vertical circulation at an ocean front. *Journal of Physical Oceanography*, 22, 609–625, 1992.
- Renault, L., McWilliams, J. C., and Gula, J.: Dampening of submesoscale currents by air-sea stress coupling in the Californian upwelling system. *Scientific Reports*, 8, doi: 10.1038/s41598-018-31602-3, 2018.
- Rhines, P. B.: Geostrophic turbulence. *Annual Review of Fluid Mechanics*, 11, 401–441, 1979.
- Rudnick, D. L.: Intensive surveys of the Azores front 2. Inferring the geostrophic and vertical velocity fields. *Journal of Geophysical Research*, 101, C7, 16291–16303, 1996.
- Shakespeare, C. J.: Spontaneous generation of internal waves. *Physics Today*, 72, 6, 34, doi: 10.1063/PT.3.4225, 2019.
- Shakespeare, C. J., and Taylor, J. R.: The spontaneous generation of inertia-gravity waves during frontogenesis forced by large strain: theory. *Journal of Fluid Mechanics*, 757, 817–853, doi: 10.1017/jfm.2014.514, 2014.
- Shchepetkin, A. F., and Williams, J. C.: A family of finite-volume methods for computing pressure gradient force in an ocean model with a topography-following vertical coordinate. Available at <http://www.atmos.ucla.edu/~alex/ROMS/pgf1A.ps>, 24 pp., last access 10 March 2017, 2001.
- Shchepetkin, A. F., and McWilliams, J. C.: The Regional Ocean Modeling System (ROMS): A split-explicit, free-surface, topography following coordinates ocean model. *Ocean Modelling*, 9, 347–404, doi: 10.1016/j.ocemod.2004.08.002, 2005.
- Shcherbina, A., D’Asaro, E., Lee, C., Klymak, J., Molemaker, M., and McWilliams, J. C.: Statistics of vertical vorticity, divergence, and strain in a developed submesoscale turbulence field. *Geophysical Research Letters*, 40, 4706–4711, doi: 10.1002/grl.50919, 2013.
- Shcherbina, A., Sundermeyer, M. A., Kunze, E., D’Asaro, E., Badin, G., Birch, D., Brunner-Suzuki, A.-M. E. G., Callies, J., Kuebel Cervantes, B. T., Claret, M., Concannon, B., Early, J., Ferrari, R., Goodman, L., Harcourt, R. R., Klymak, J. M., Lee, C. M., Lelong, M.-P., Devine, M. D., Lien, R.-C., Mahadevan, A., McWilliams, J. C., Molemaker, M. J., Mukherjee, S., Nash, J. D., Özgökmen, T., Pierce, S. D., Ramachandran, S., Samelson, R. M., Sanford, T. B., Shearman, R. K., Skillingstad, E. D., Smith, K. S., Tandon, A., Taylor, J. R., Terray, E. A., Thomas, L. N., and Ledwell, J. R.: The LatMix Summer Campaign, *Bulletin of the American Meteorological Society*, 96(8), 1257–1279, doi: 10.1175/BAMS-D-14-00015.1, 2015.
- Smedman, A.-S., Gryning, S.-E., Högström, U., Rutgersson, A., Batchvarova, E., Peters, G., Hennemuth, B., Tammelin, B., Hyvönen, R., Omstedt, A., Michelson, D., Andersson, T., and Clemens, M.: Precipitation and evaporation budgets over the Baltic Proper: observations and modelling. *Journal of Atmospheric and Ocean Science*, 10(3), 163–191, doi: 10.1080/17417530500513756, 2005.
- Song, Y. and Haidvogel, D. B.: A semi-implicit ocean circulation model using a generalized topography-following coordinate system. *Journal of Computational Physics*, 115, 1, 228–244, 1994.
- Stamper, M. A., and Taylor, J. R.: The transition from symmetric to baroclinic instability in the Eady model. *Ocean Dynamics*, 67, 65–80, doi: 10.1007/s10236-016-1011-6, 2017.

- Sullivan, P. P., and McWilliams, J. C.: Frontogenesis and frontal arrest of a dense filament in the oceanic surface boundary layer. *Journal of Fluid Mechanics*, 837, 341–380, doi: 10.1017/jfm.2017.833, 2018.
- 5 [Tavri, A., Singha, S., Lehner, S., and Topouzelis, K.: Observations of sub-mesoscale eddies over Baltic Sea using TerraSAR-X and oceanographic data. ESA “Living Planet” Symposium, Prague, Czech Republic, 9–13 May, 2016.](#)
- Taylor, J. R., and Ferrari, R.: On the equilibrium of a symmetrically unstable front via a secondary shear instability. *Journal of Fluid Mechanics*, 22, 103–113, doi: 10.1017/S0022112008005272, 2009.
- Thomas, L. N., Tandon, A., and Mahadevan, A.: Submesoscale processes and dynamics. In: Hecht, M.W., and Hasumi, H. (Eds.) *Ocean Modeling in an Eddying Regime*, Geophysical Monograph Series, 177, 17–38, doi: 10.1029/177GM04, 2008.
- 10 Thomas, L. N., Taylor, J. R., Ferrari, R., and Joyce, T. M.: Symmetric instability in the Gulf Stream. *Deep-Sea Research II*, 91, 96–110, doi: 10.1016/j.dsr2.2013.02.025, 2013.
- Thompson, L.: Ekman layers and two-dimensional frontogenesis in the upper ocean. *Journal of Geophysical Research*, 105, C3, 6437 – 6451, 2000.
- Umlauf, L., and Burchard, H.: A generic length-scale equation for geophysical turbulence models. *Journal of Marine Research*, 61, 235–265, 15 2003.
- Väli, G., Zhurbas V.M., Laanemets J., Lips U.: Clustering of floating particles due to submesoscale dynamics: a simulation study for the Gulf of Finland, Baltic Sea. *Fundamentalnaya i Prikladnaya gidrofizika*, 11(2), 21–35, doi: 10.7868/S2073667318020028, 2018.
- Väli, G., Zhurbas, V., Lips, U., and Laanemets, J.: Submesoscale structures related to upwelling events in the Gulf of Finland, Baltic Sea (numerical experiments), *Journal of Marine Systems*, 171(SI), 31–42, <http://dx.doi.org/10.1016/j.jmarsys.2016.06.010>, 2017.
- 20 Vitousek, S., and Fringer, O. B.: Physical vs. numerical dispersion in nonhydrostatic modeling. *Ocean Modelling*, 40, 72–86, doi: 10.1016/j.ocemod.2011.07.002, 2011.
- [Vortmeyer-Kley, R., Holtermann, P., Feudel, U., and Gräwe, U.: Comparing Eulerian and Lagrangian eddy census for a tide-less semi-enclosed basin, the Baltic Sea. *Ocean Dynamics*, 69, 701–717, doi: 10.1007/s10236-019-01269-z, 2019.](#)
- Wadzuk, B. M., and Hodges, B. R.: Hydrostatic versus nonhydrostatic Euler-equation modeling of nonlinear internal waves. *Journal of Engineering Mechanics*, 1069–1080, doi: 10.1061/(ASCE)0733-9399(2009)135:10(1069), 2009.
- 25 Wilcox, D. C.: Reassessment of the scale-determining equation for advanced turbulence models. *AIAA Journal*, 26, 1299–1310, 1988.
- Zatsepin, A. G., Denisov, E. S., Emelyanov, S. V.: Effect of bottom slope and wind on the near-shore current in a rotating stratified fluid: laboratory modeling for the Black Sea, *Oceanology* 45 (Suppl. 1), S13–S26, 2005.
- Zhong, Y., Bracco, A., Tian, J., Dong, J., Zhao, W., and Zhang, Z.: Observed and simulated submesoscale vertical pump of an anticyclonic eddy in the South China Sea. *Scientific Reports*, 7:44011, doi: 10.1038/srep44011, 2017.
- 30 Zhurbas, V., Laanemets, J., and Vahtera, E.: Modeling of the mesoscale structure of coupled upwelling/downwelling events and the related input of nutrients to the upper mixed layer in the Gulf of Finland, Baltic Sea. *Journal of Geophysical Research Oceans*, 113, C05004, doi: 10.1029/2007JC004280, 2008.
- [Zhurbas, V., Väli, G., and Kuzmina, N.: Rotation of floating particles in submesoscale cyclonic and anticyclonic eddies: a model study for the southeastern Baltic Sea. *Ocean Science*, 15, 1691–1705, doi: 10.5194/os-15-1691-2019, 2019.](#)

Table 1. Parameter settings and used equations common to all ROMS setups.

* as described by Onken (2017)

Parameter	Units	Value	Meaning
K	1	10	number of vertical layers
V_{tr}	N/A	2	transformation equation
V_{str}	N/A	1	stretching function
θ_s	1	5	surface control parameter
θ_b	1	0.4	bottom control parameter
h_c	m	10	critical depth
A_V^T	m^2s^{-1}	4×10^{-5}	vertical mixing coefficient for tracers*
A_V^M	m^2s^{-1}	1×10^{-5}	vertical mixing coefficient for momentum*
Δt_{fast}	1	20	Number of barotropic time-steps between each baroclinic time step

Table 2. Parameter settings and properties of the R500 and R100 setups.

Parameter/Property	Units	R500	R100	Meaning
Δx	m	500	100	nominal zonal grid size
Δy	m	500	100	nominal meridional grid size
lon_{west}		13°30' W	14°12' W	western boundary of model domain
lon_{east}		16°30' W	15°48' W	eastern boundary of model domain
lat_{south}		53°54' N	54°18' N	southern boundary of model domain
lat_{north}		55°30' N	55°12' N	northern boundary of model domain
N_x	1	386	1033	number of tracer grid points (zonal)
N_y	1	356	1004	number of tracer grid points (meridional)
domain size	km^2	193×178	103×100	
Δt	s	150	30	baroclinic time step
A_H^T	m^4s^{-1}	5×10^5	10^3	bi-harmonic eddy diffusivity coefficient
A_H^M	m^4s^{-1}	10^3	N/A	bi-harmonic eddy viscosity coefficient
A_H^M	m^2s^{-1}	N/A	10^{-2}	mono-harmonic eddy viscosity coefficient
vertical mixing scheme	N/A	GLS	KPP	
rx_0	1	0.16	0.07	stability condition after Haidvogel et al. (2000)
rx_1	1	1.75	0.84	stability condition after Haney (1991)

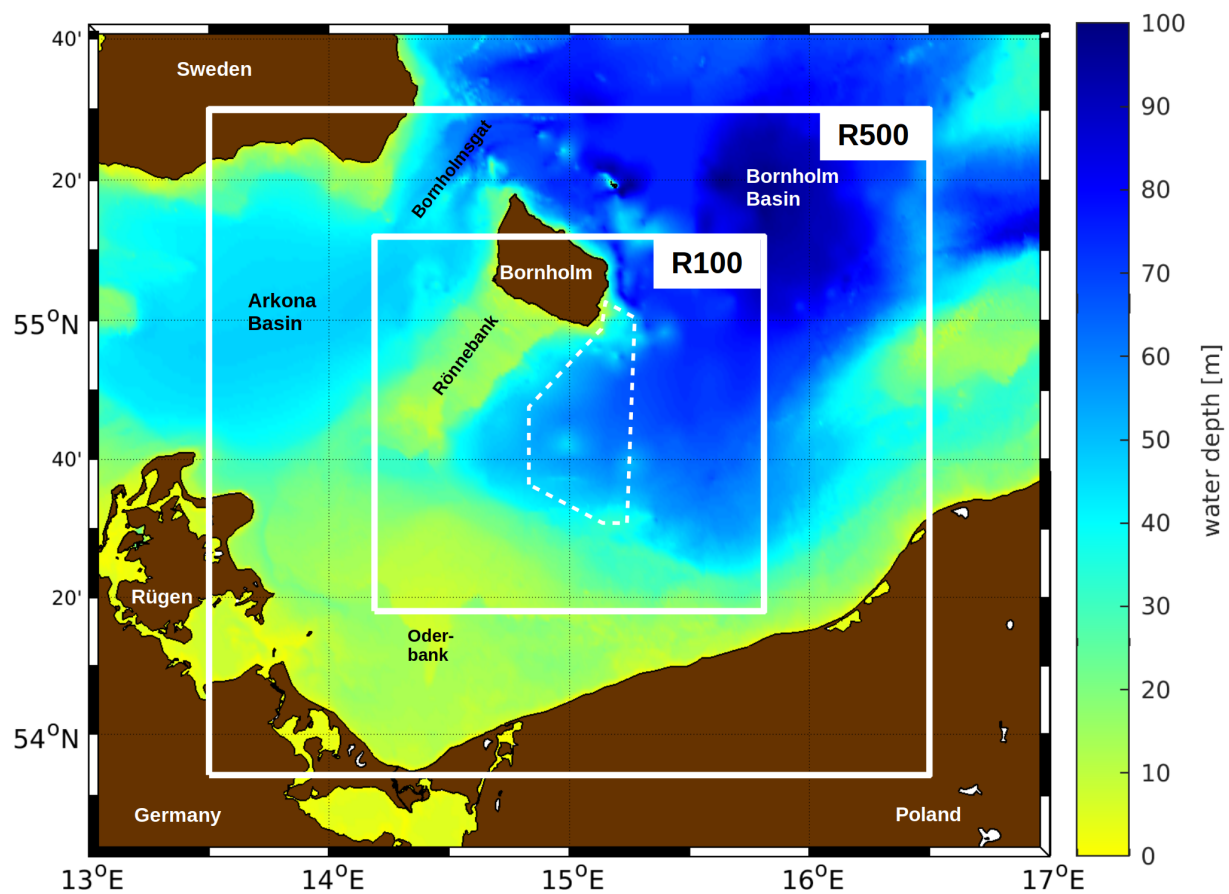


Figure 1. The R500 and R100 model domains in the western Baltic Sea. The approximate experimental area of the “Expedition Clockwork Ocean” is indicated by the dashed polygon.

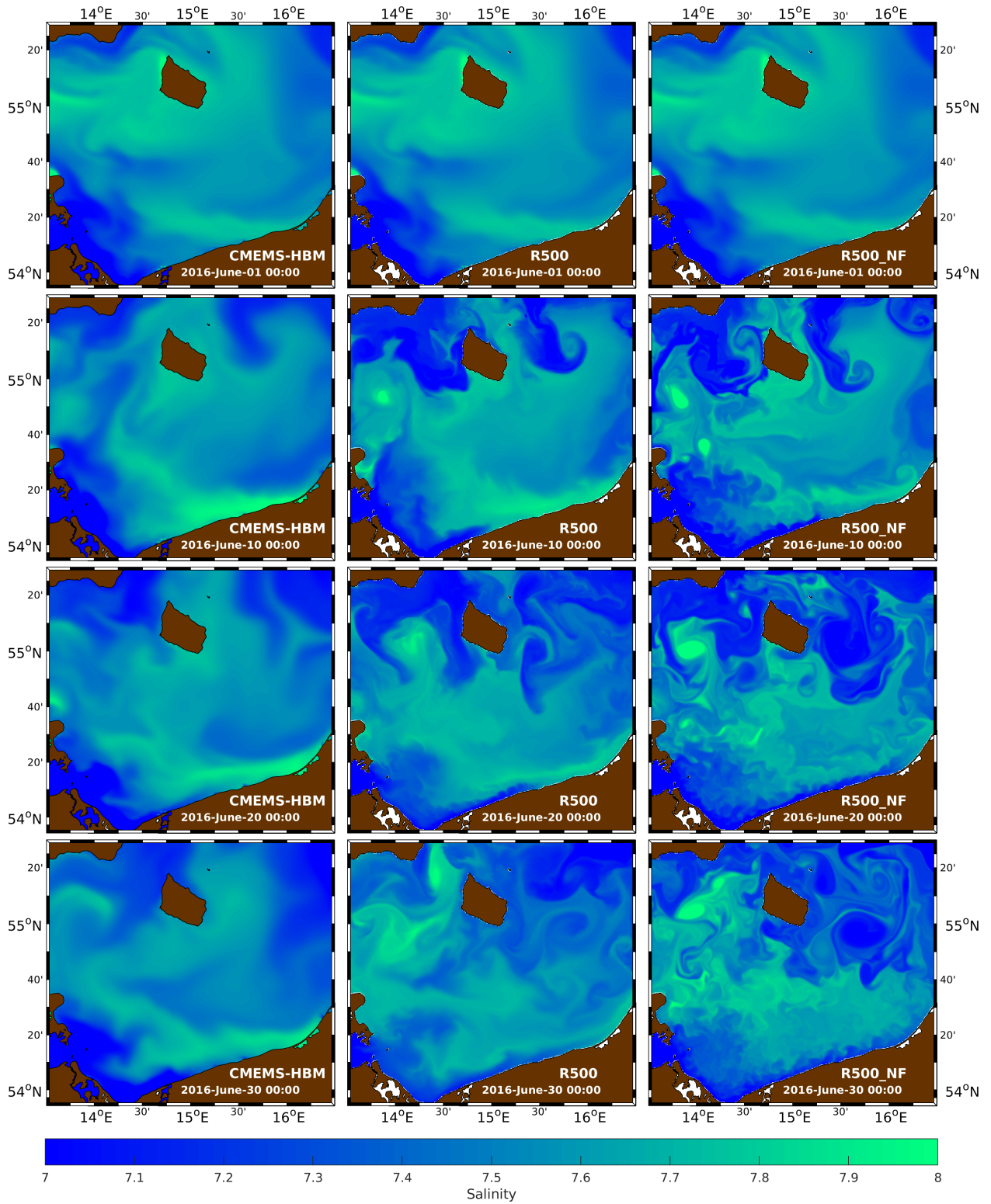


Figure 2. Top-layer salinity in CMEMS-HBM (left column), R500 (centre), and R500_NF (right) for 1, 10, 20, and 30 June. The CMEMS-HBM fields are interpolated onto the R500 horizontal grid. Due to the coarser horizontal grid of CMEMS-HBM, inland lakes are not resolved and salinity values were assigned to places that are dry in R500. **31**

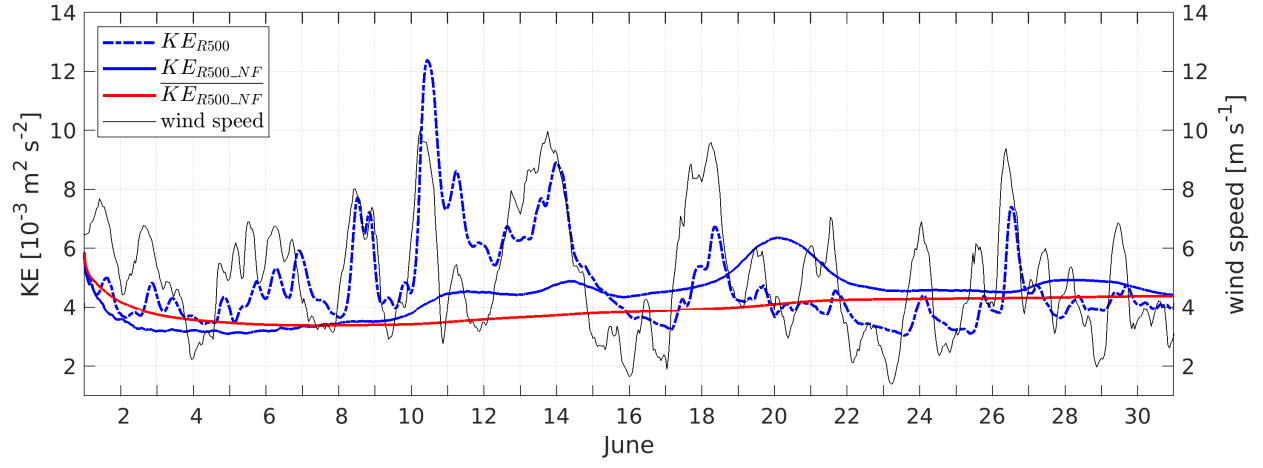


Figure 3. Instantaneous (KE_{R500} , KE_{R500_NF}) and cumulatively averaged ($\overline{KE_{R500_NF}}$) kinetic energy per unit mass of the model runs R500 and R500_NF. The wind speed is shown as black curve. All quantities are averaged over the model domain.

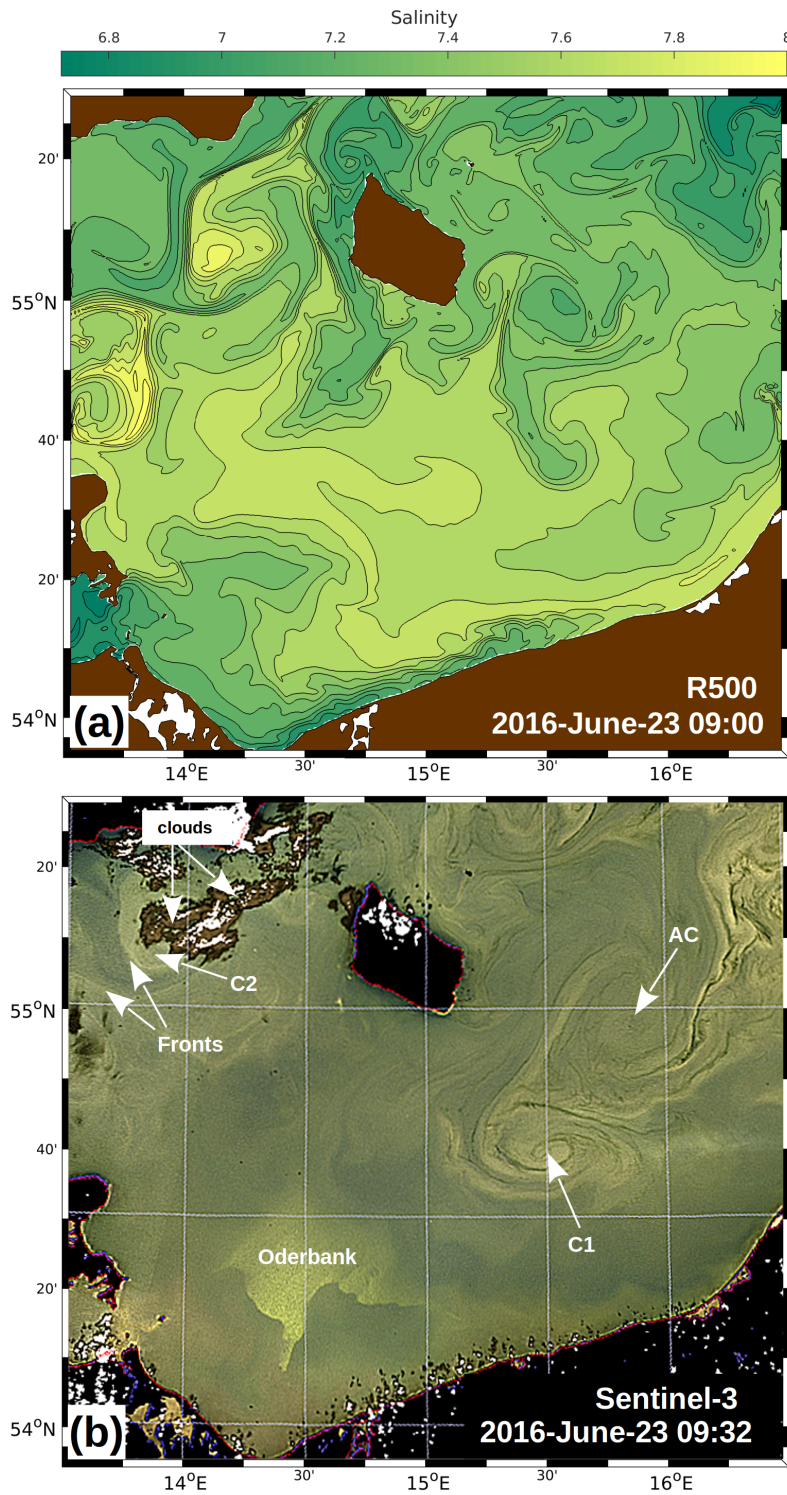


Figure 4. (a) Top-layer salinity of the R500 model on 23 June 09:00. (b) RGB composite from the Ocean and Land Colour Instrument of ESA satellite Sentinel-3 for the R500 domain on 23 June 09:32. The original image was manually adjusted in order to fit to the Mercator projection used in (a). C1, C2, and AC refer to the signatures of cyclonic and anticyclonic eddies, respectively. For the Oderbank, cf. Fig. 1.

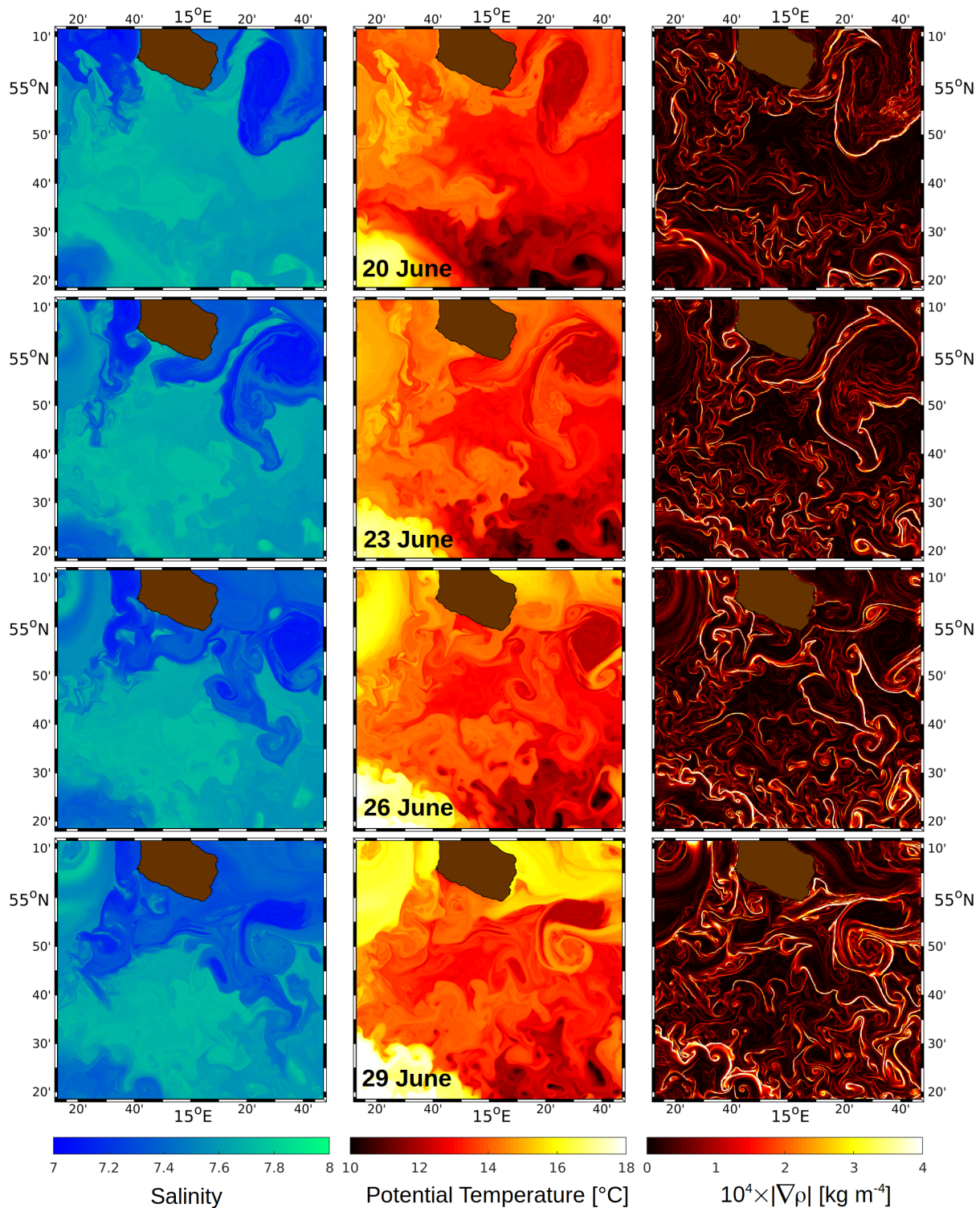


Figure 5. R100: top-layer salinity (left column), potential temperature (centre), and the absolute horizontal gradient of potential density (right) on 20, 23, 26 and 29 June. The upper end of the colour axis of $|\nabla \rho|$ is limited to 4×10^{-4} kg m⁻⁴ to distinguish higher gradients from the dark background.

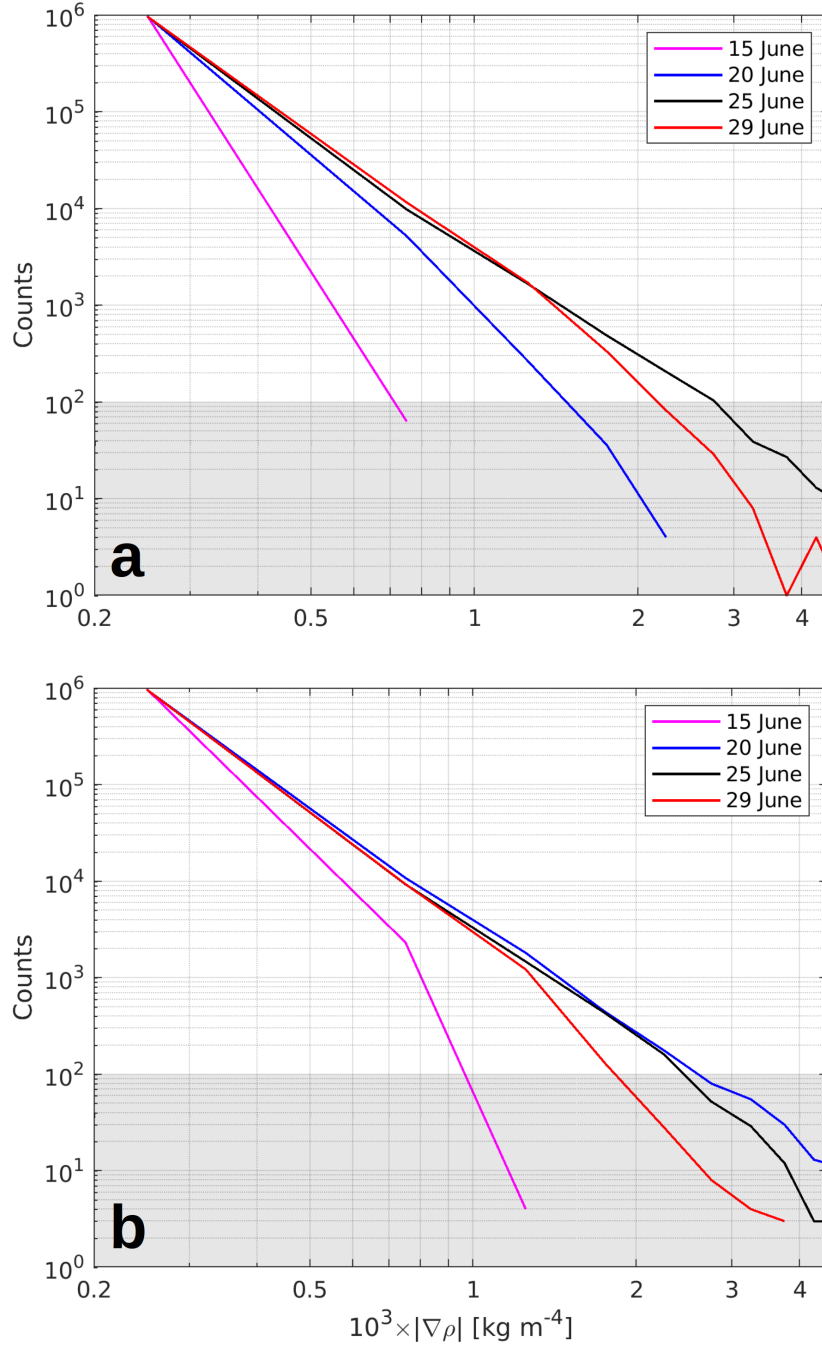


Figure 6. R100: frequency distribution of $|\nabla\rho|$ in the top layer. The initial and the open boundary conditions for R100 were provided by (a) R500 and (b) R500_NF, respectively. The values were binned in 10 intervals of $0.5 \times 10^{-3} \text{ kg m}^{-4}$ width between 0 and $5 \times 10^{-3} \text{ kg m}^{-4}$. Counts < 100 (gray shaded) representing less than 0.1% of the total number of horizontal grid points were not considered as significant.

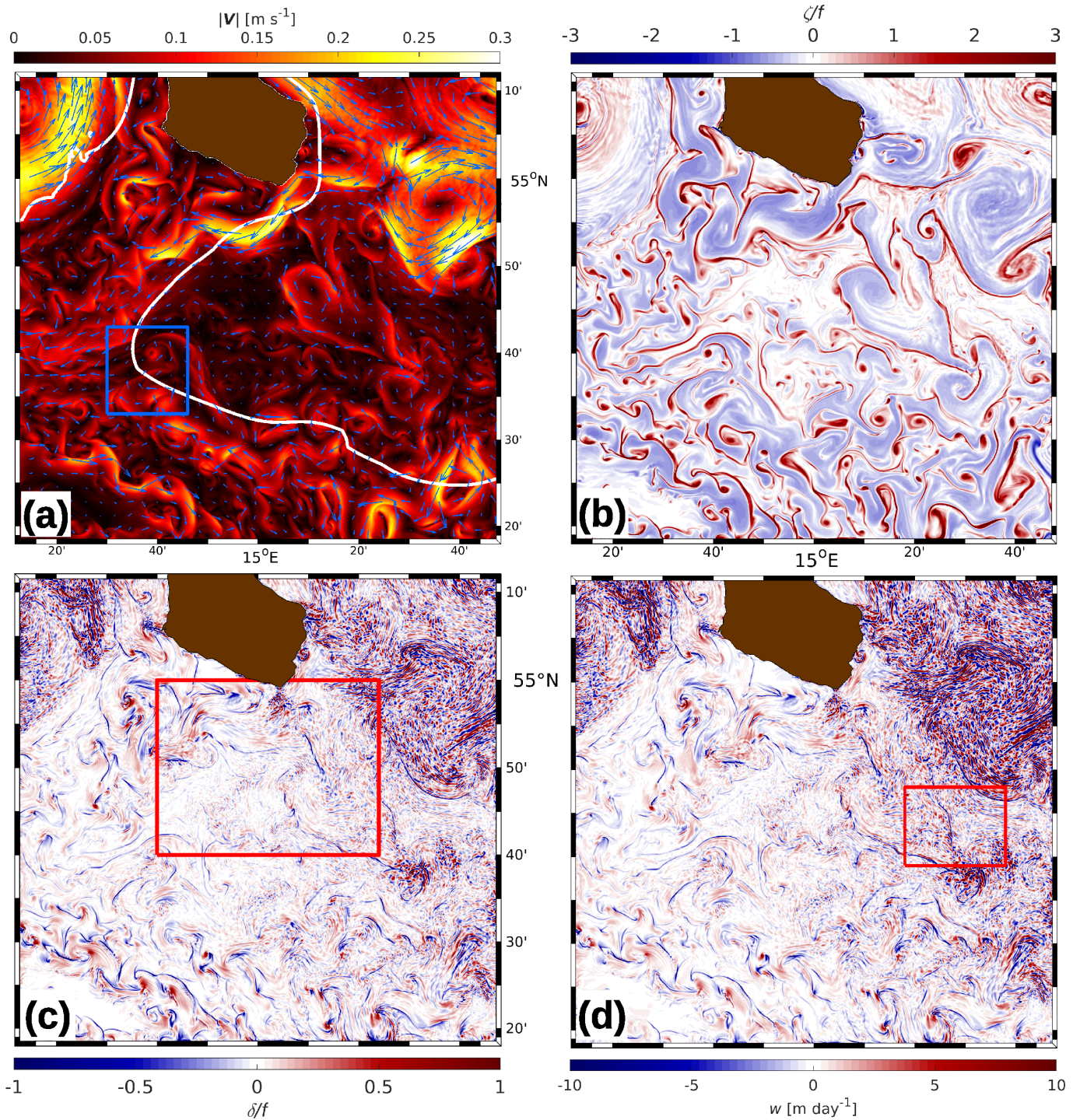


Figure 7. R100, 26 June: (a) Magnitude and direction of top-layer horizontal velocity V (vectors are plotted at 3-km resolution), (b) relative vorticity ζ and (c) horizontal divergence δ , each scaled by f , (d) vertical velocity w at 5-m depth. The white line in (a) is the 40-m depth contour. The blue box in (a) refers to the zoomed area shown in Figs. 11 and 12, the box in (c) is the zoomed area of Fig. 8, and the box in (d) is the zoom shown in Fig. 15.

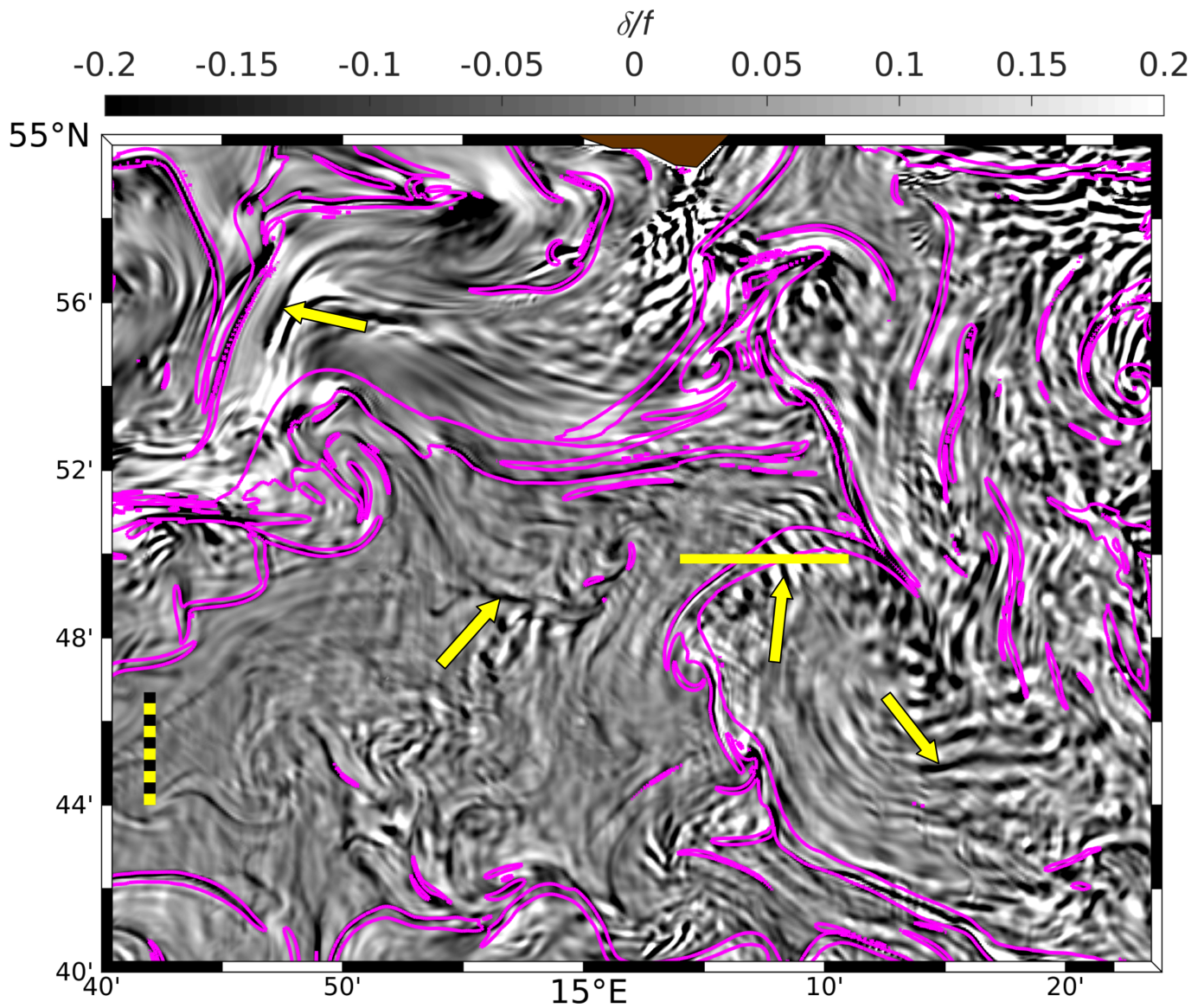


Figure 8. R100, 26 June: zoom of f -scaled horizontal divergence δ (grayscale image, for the position of the zoomed area see Fig. 7c). Bright areas indicate divergent flow, convergences appear dark. The magenta lines show the $|\nabla\rho| = 10^{-4} \text{ kg m}^{-4}$ contours. The yellow arrows likely mark internal wave packages as discussed in the text. The horizontal yellow line is the position of the section shown in Fig. 9. The dashed ruler represents a distance of 5 km

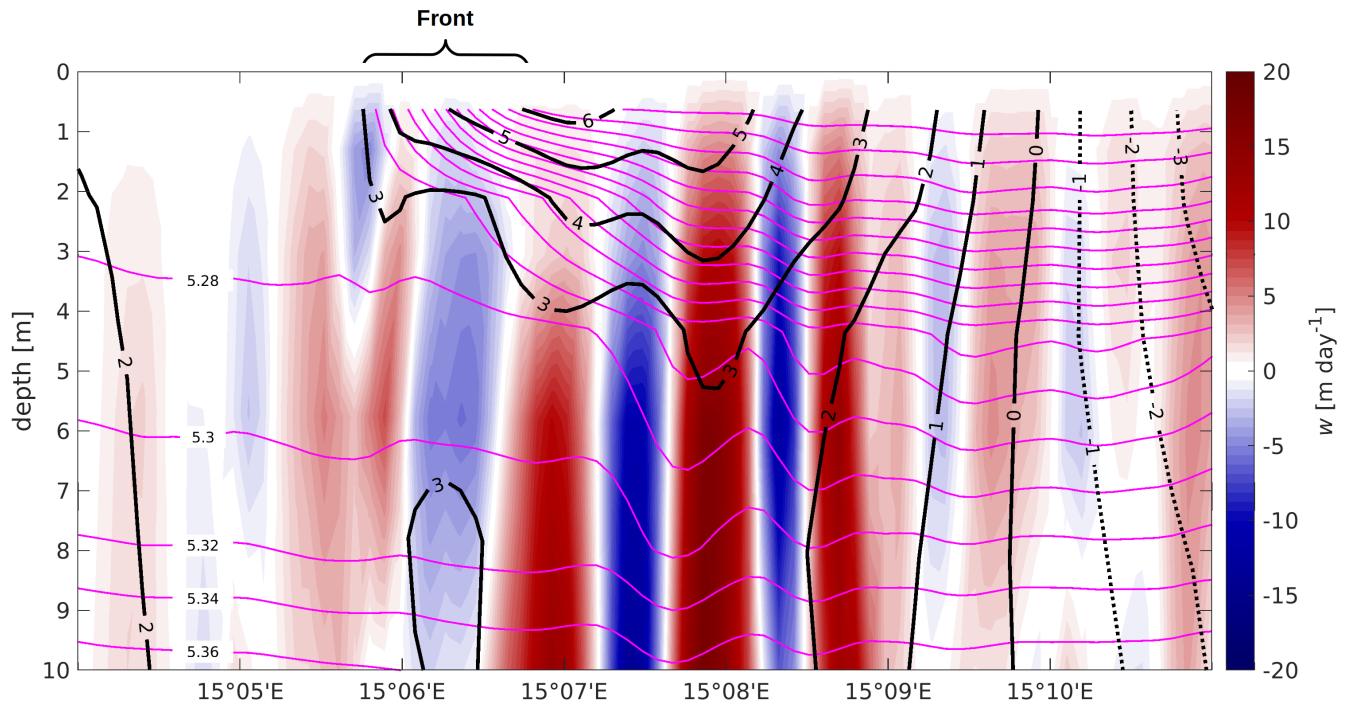


Figure 9. R100, 26 June: zonal section of vertical velocity w at $54^{\circ}49.9'$ N. Magenta contours indicate potential density anomaly σ_{θ} , bold solid and dotted contours are isotachs of the meridional velocity component v [cm s^{-1}]. The position of the section is marked in Fig. 8.

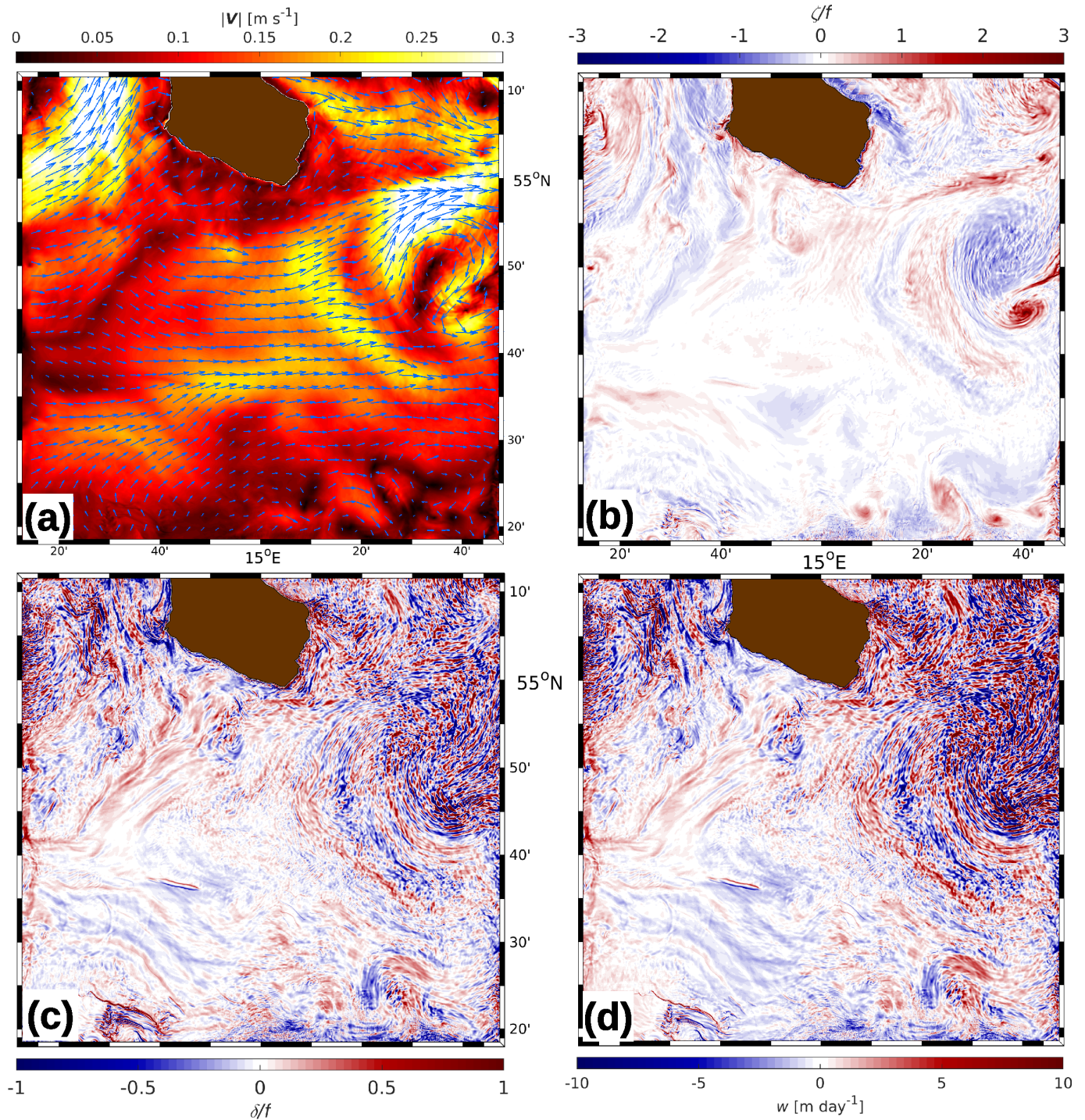


Figure 10. R100 with full atmospheric forcing on 26 June: (a) Magnitude and direction of top-layer horizontal velocity \mathbf{V} (vectors are plotted at 3-km resolution), (b) relative vorticity ζ and (c) horizontal divergence δ , each scaled by f , (d) vertical velocity w at 5-m depth. For all subplots, the same color scaling was used as in Fig. 7.

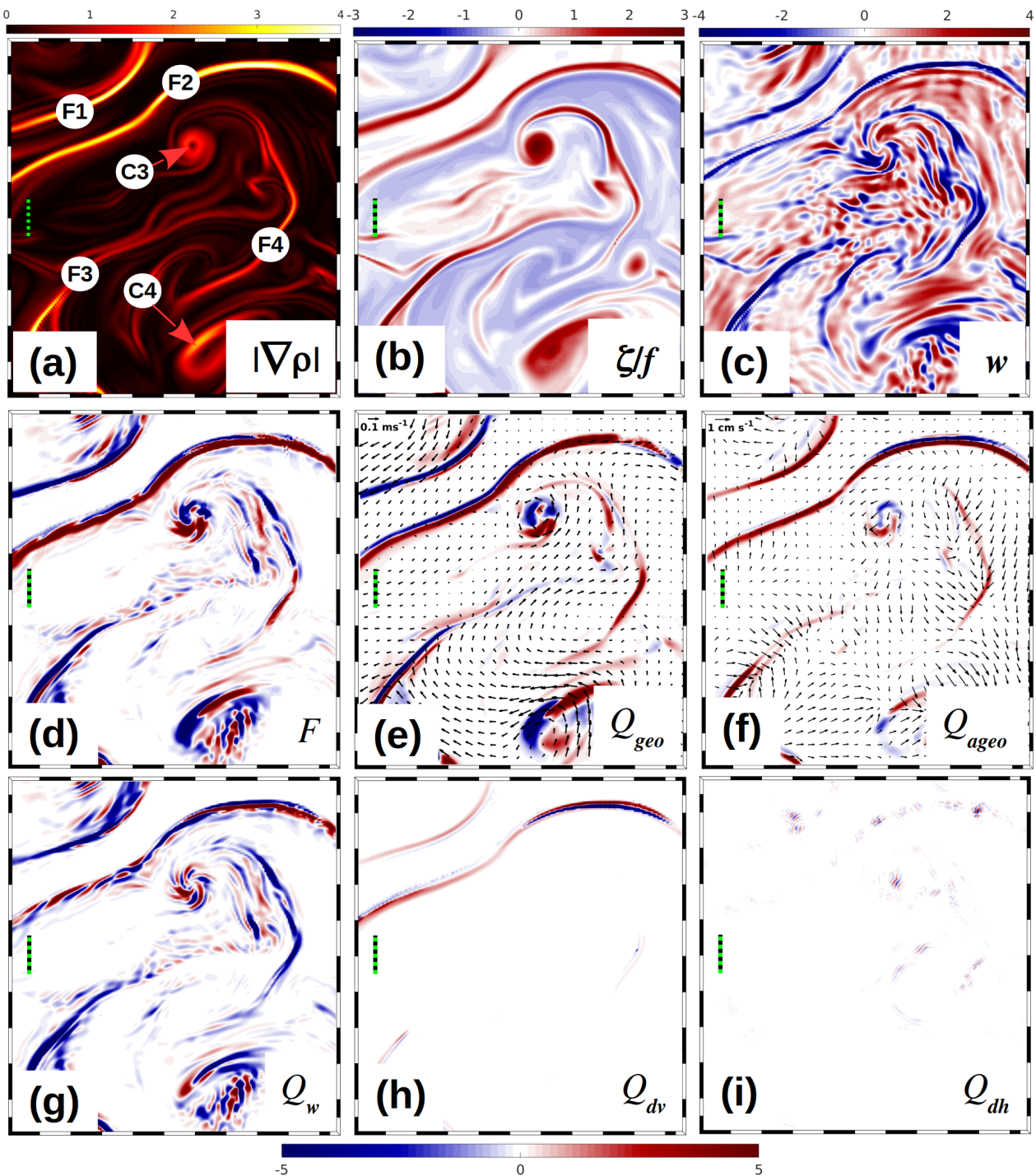


Figure 11. R100: near-surface properties on 26 June within the blue box depicted in Fig. 7a. (a) Absolute horizontal density gradient $|\nabla\rho|$ [$10^{-4} \text{ kg m}^{-4}$], and (b) scaled relative vorticity ζ/f in the top layer, (c) vertical velocity w [m day^{-1}] at the base of the top layer. (d) – (i) The frontal tendency F and the components of the tendency equation Q_{geo} , Q_{ageo} , Q_w , Q_{dv} , Q_{dh} [$10^{-13} \text{ kg}^{-2} \text{ m}^{-8} \text{ s}^{-1}$] at 2-m depth. Red marks frontogenesis, blue frontolysis. For the labels F1–F4, C3, C4 see text. The dashed rulers represent a distance of 2 km, vectors in (e) and (f) are drawn at 600-m intervals.

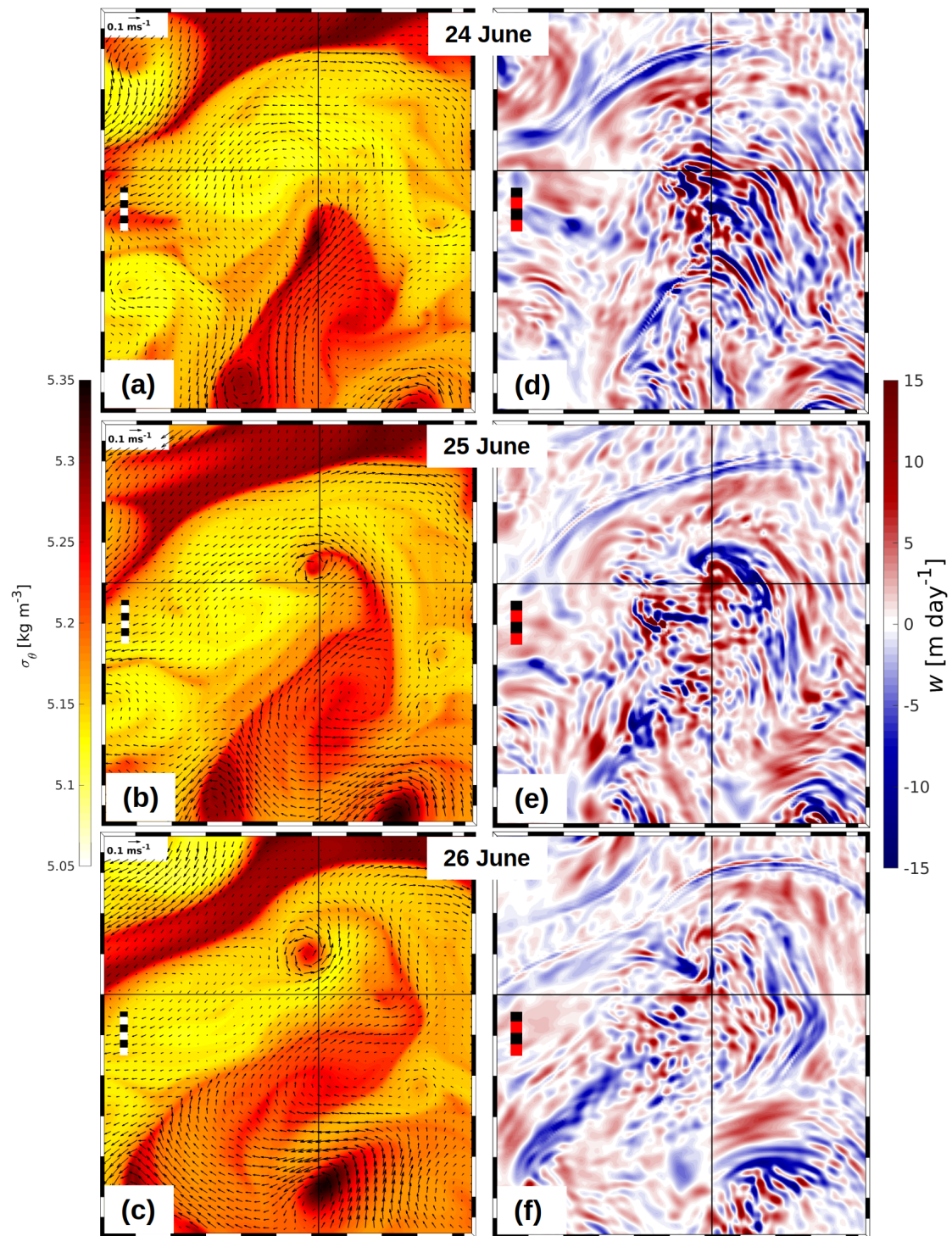


Figure 12. R100: (a)–(c) temporal evolution of potential density anomaly σ_θ in the top layer with vectors of total velocity V drawn at 400-m resolution, (d)–(f) corresponding vertical velocity w at 5-m depth; upwelling is positive. The area shown is indicated by the blue box in Fig. 7a. The crosshair tags the same position in all subplots. The dashed rulers represent a distance of 2 km.

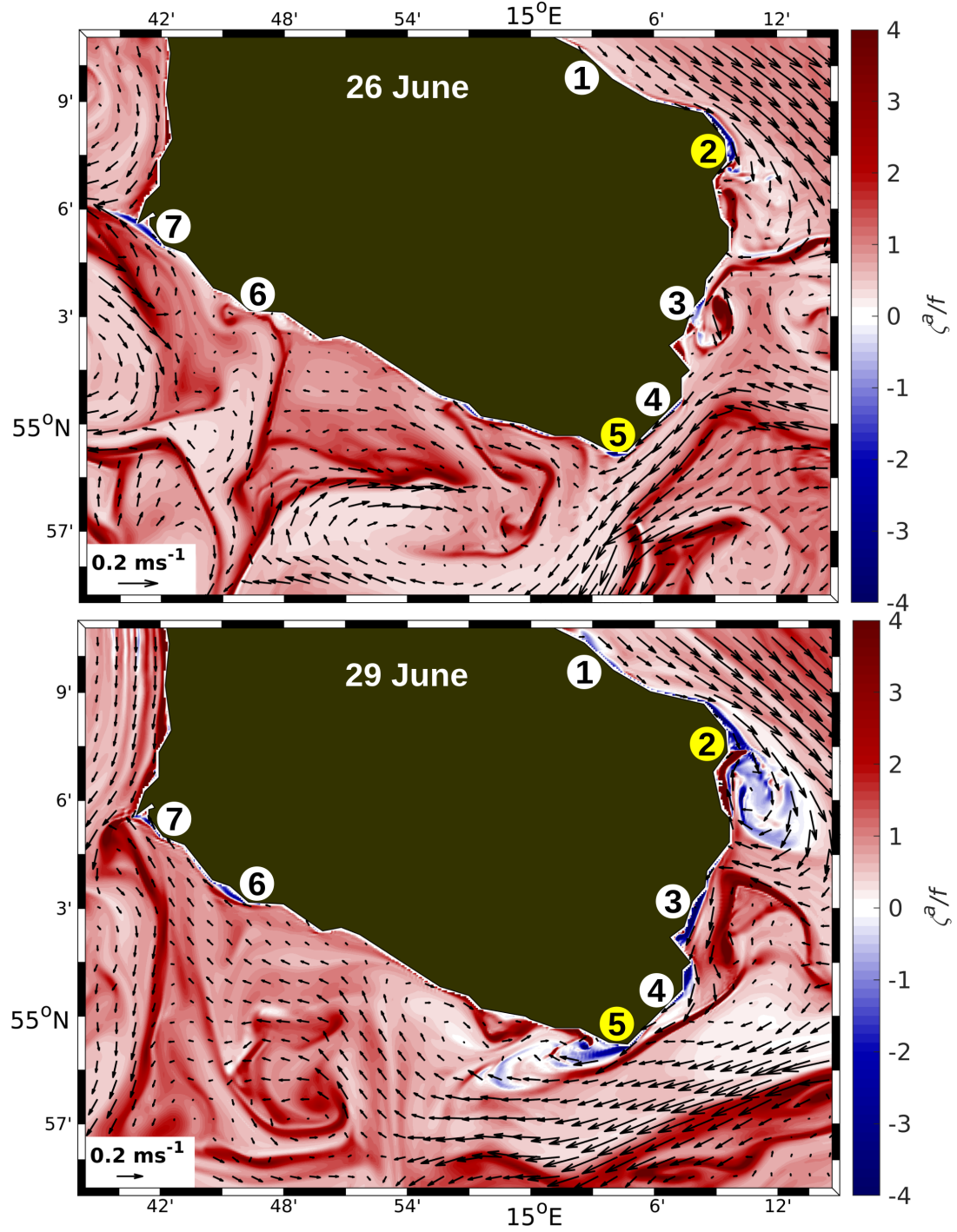


Figure 13. R100: normalized absolute vorticity, ζ^a/f , in the surface layer of the waters around Bornholm on 26 and 29 June. Encircled numbers indicate near-coastal locations of $\zeta^a/f < 0$. Yellow circles mark locations where inertial instabilities tend to grow offshore.

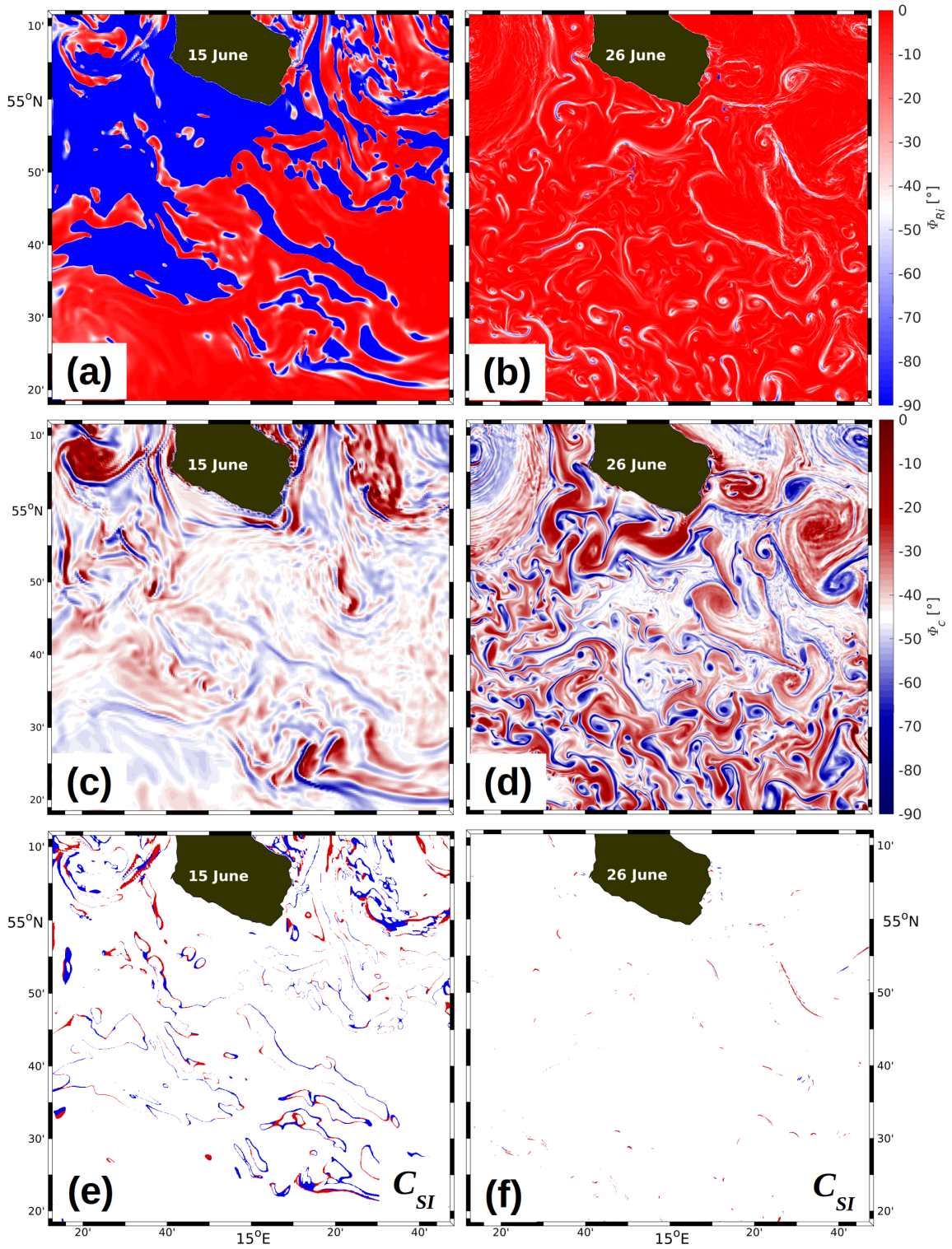


Figure 14. R100: (a, b) ϕ_{Ri} , (c, d) ϕ_c , and (e, f) C_{SI} at 2-m depth on 15 (left column) and 26 June (right). (e) and (f) are logical maps indicating where the condition for symmetric instability, C_{SI} , is satisfied in regions of cyclonic (red) and anticyclonic (blue) absolute vorticity, according to eqs. (17) and (18), respectively. For explanation of the other symbols see text.

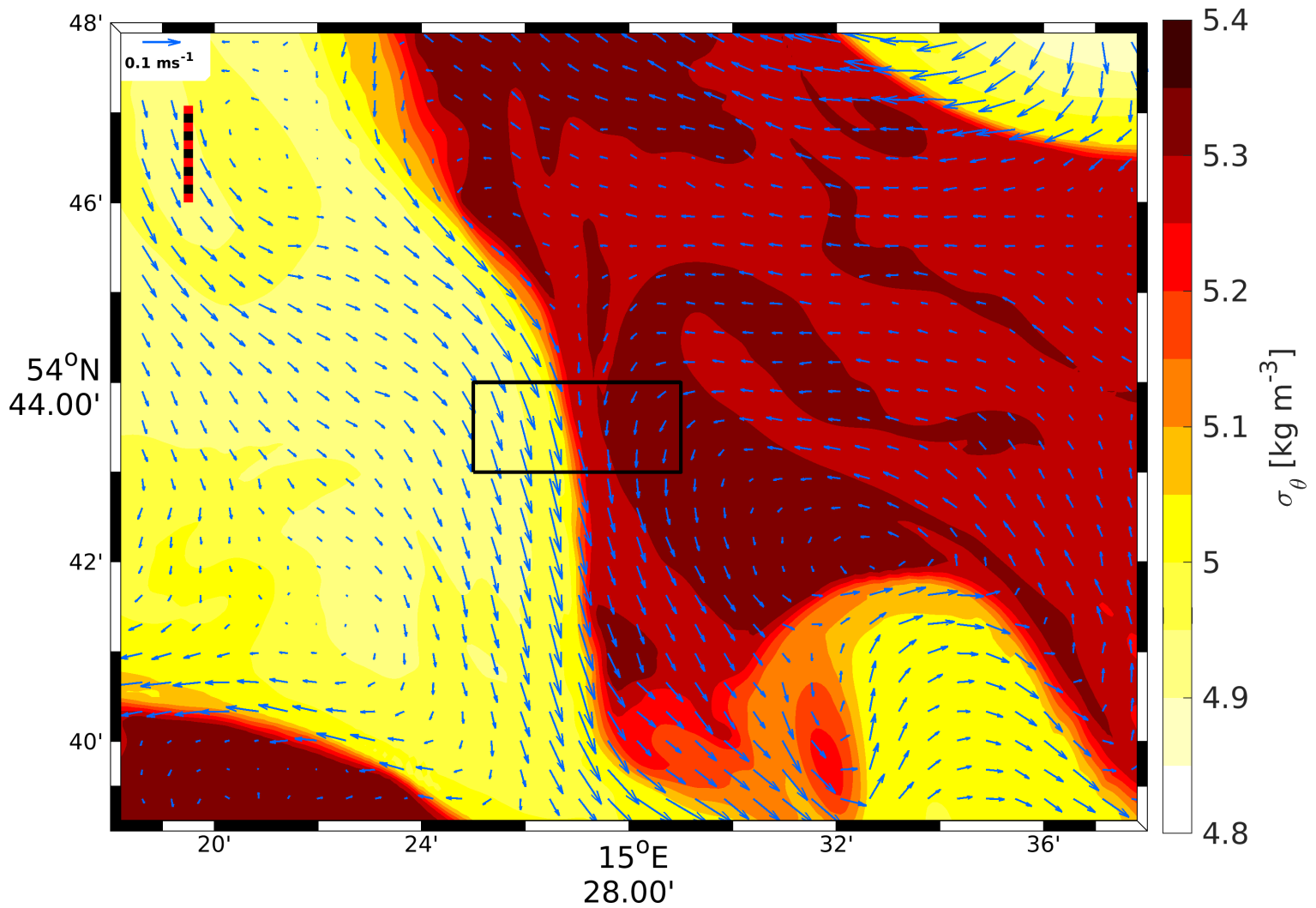


Figure 15. R100, 26 June: Potential density anomaly σ_θ in the top layer with total velocity \mathbf{V} drawn at 600-m resolution. For the position of the area, see the red box in Fig. 7d. The black box indicates the position of the maps shown in Fig. 16a–e. The dashed ruler represents a distance of 2 km.

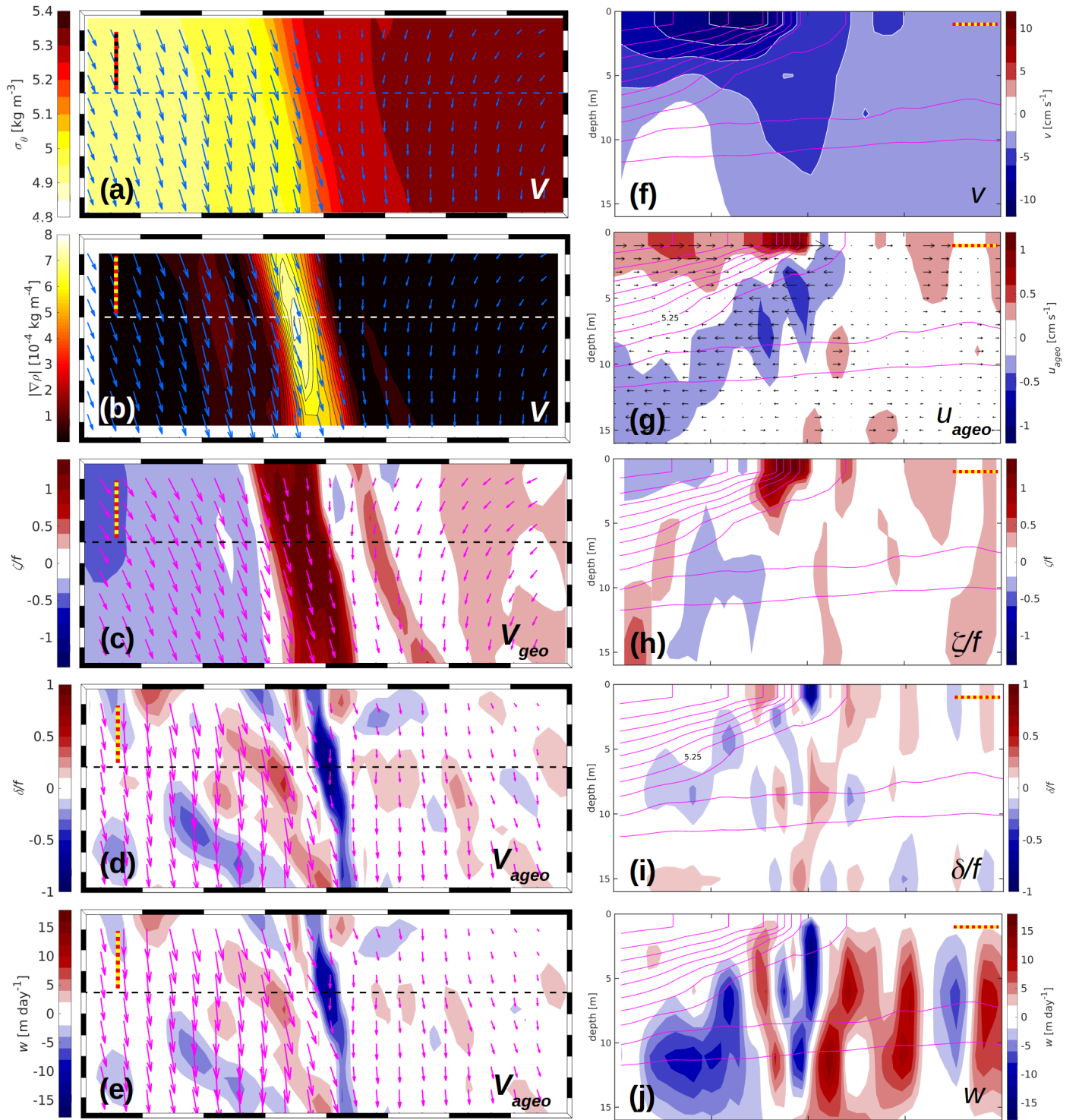


Figure 16. R100, 26 June: maps of dynamical quantities within the black box in Fig. 15. (a) σ_θ and \mathbf{V} , (b) $|\nabla\rho|$ and \mathbf{V} , (c) ζ/f and \mathbf{V}_{geo} , (d) δ/f and \mathbf{V}_{ageo} in the top layer, and (e) w and \mathbf{V}_{ageo} at the bottom of the top layer. Velocity vectors are drawn at a resolution of 200 m. Vertical sections of (f) v , (g) u_{ageo} , (h) ζ/f , (i) δ/f , and (j) w . Contour lines of potential density anomaly σ_θ are magenta and spaced at the same intervals as in (a). The horizontal dashed lines in the centres of (a)–(e) indicate the position of the zonal sections displayed in (f)–(j). In either subplot, the dashed rulers represent a horizontal distance of 500 m.

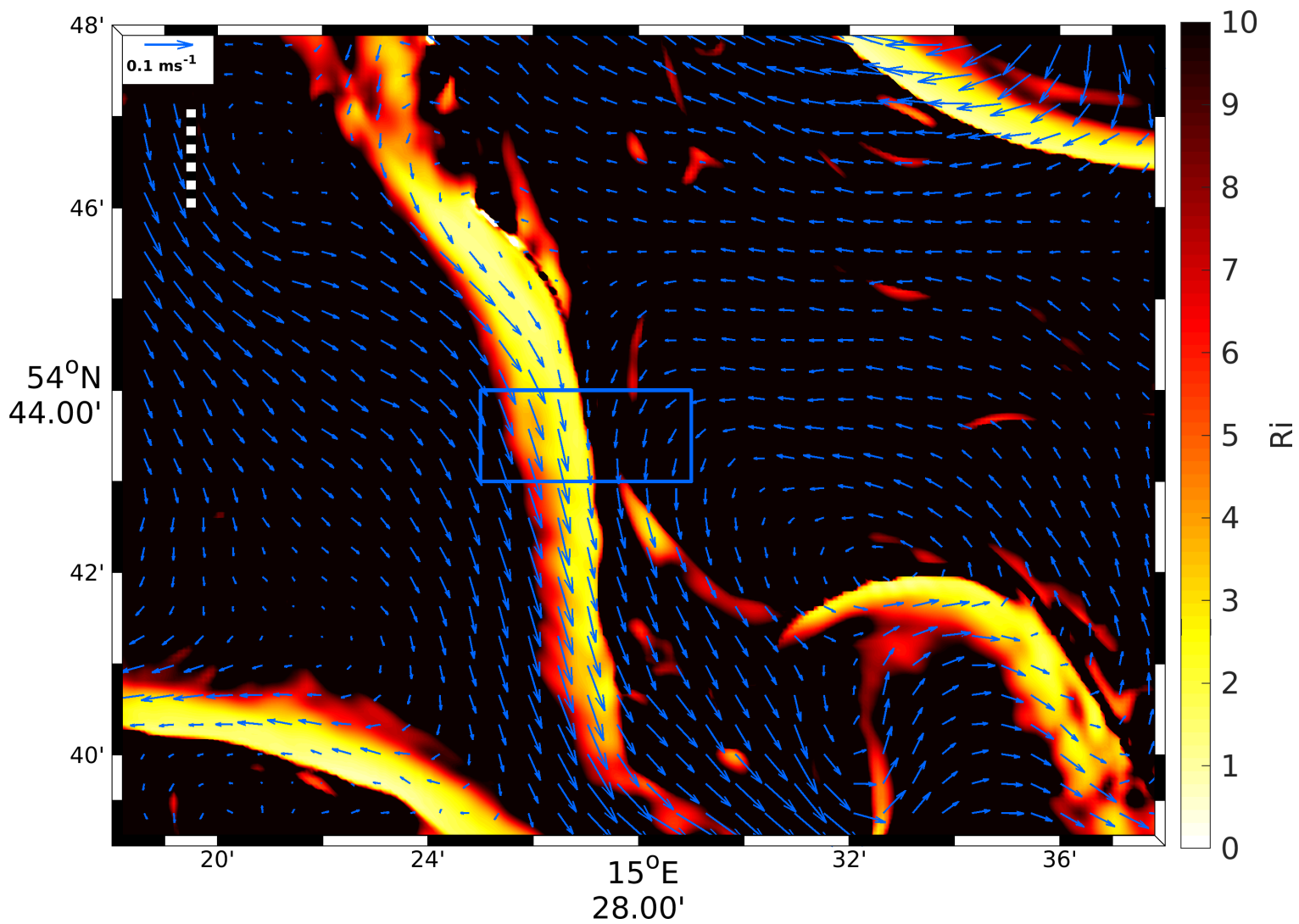


Figure 17. R100, 26 June: Richardson number Ri at 2-m depth and total top-layer velocity \mathbf{V} drawn at 600-m resolution. For the position of the area, see the red box in Fig. 7d. The magenta box indicates the position of the maps shown in Fig. 16a–e. It is identical with the black box in Fig. 15. The dashed ruler represents a distance of 2 km.

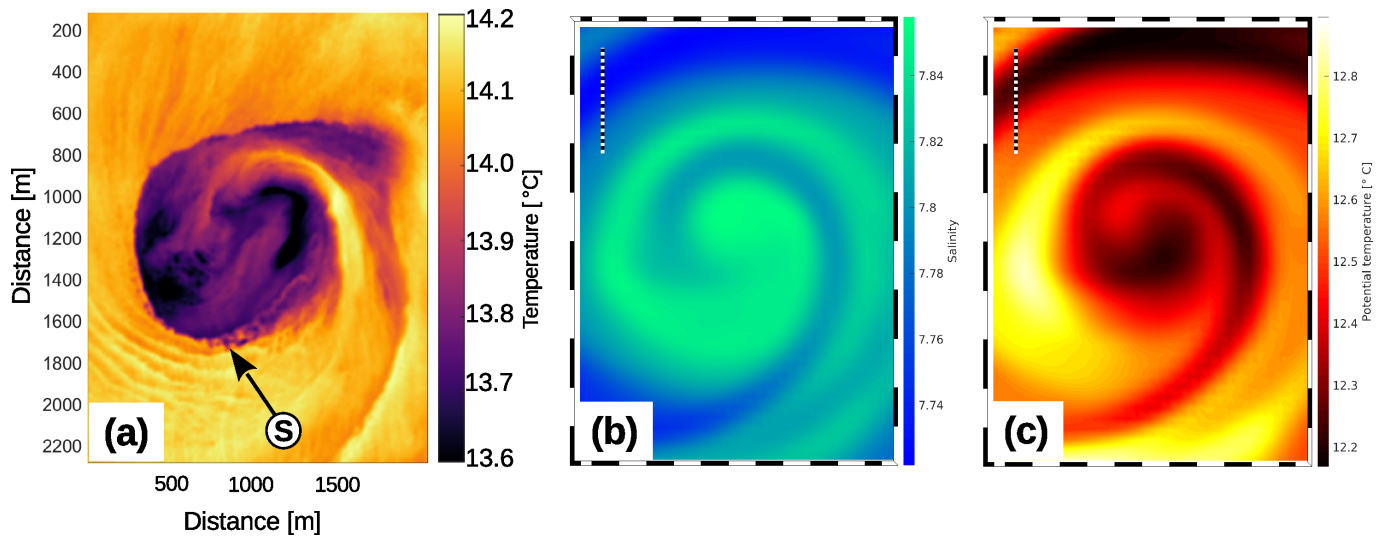


Figure 18. Tracer patterns of submesoscale eddies. (a) Observed sea surface temperature of a cyclonic eddy in the Southern California Counter Current. The image was taken on 1 February 2013 at 20:34 in the framework of the SubEx experiment (Marmorino et al., 2018). (b) Modelled salinity and (c) potential temperature of the cyclone C3 on 26 June at 15-m depth (cf. Figs. 11 and 12). Cold water spots in (a) are denoted by “S”. The dashed rulers in (b) and (c) represent a distance of 1 km.